# Experimental Testing and Analytical Modelling of Single and Double Post-Tensioned CLT Shear Walls

Justin R. Brown[a]*, Minghao Li[a], Alessandro Palermo[a], Stefano Pampanin[b], Francesco Sarti[c], Roger Nokes[a]

[a] Department of Civil and Natural Resources Engineering, University of Canterbury, New Zealand

[b] Department of Structural and Geotechnical Engineering, Sapienza University of Rome, Italy

[c] PTL| Structural Consultants, Christchurch, New Zealand

## ABSTRACT

Post-tensioned (PT) timber technology - also called Pres-Lam technology - can provide increased strength/stiffness for mass timber seismic load resisting systems while also providing energy dissipation and re-centering capabilities. Initial experimental tests and practical implementation on PT timber structures in the past 15 years primarily utilized laminated veneer lumber (LVL), with some glulam and cross-laminated timber (CLT) prototypes and real-case applications, and their analytical prediction models were extended and adapted from precast concrete to account for unique characteristics of engineered timber. More recently, CLT has emerged into a more dominant global mass timber product. This paper presents a large-scale experimental study on 8.6m tall PT CLT single and double wall systems. The PT double walls utilized screwed connections at the in-plane joint and U-shaped flexural plates at the foundation to provide coupling effect and energy dissipation. With screwed connections, the PT double wall partial composite action of approximately 70% was achieved and the system stiffness was almost two times that of two PT single walls without partial composite action but of equivalent length. Analytical prediction models, accounting for the peculiar controlled rocking mechanism, originally developed for PT LVL systems were adopted for PT CLT wall systems, which were found to have increased compressive toe strain variability due to the increased material inhomogeneity of CLT

* corresponding Author

with non-edge glued lamella. The timber compressive strains and unique 'end effect' bearing phenomenon was investigated for the first time with Particle Tracking Technology (PTT). Extensions to the existing PT double wall analytical prediction model were proposed and validated to capture the unique kinematic rocking mechanism where wall uplift occurs due to the strong and stiff screwed in-plane connection between individual walls.

Keywords: Timber wall structures; Post-tensioning systems; Cross-laminated timber; Re-centering systems; Particle tracking technology; Screwed connections.

## 1 INTRODUCTION

Mass timber construction in cross-laminated timber (CLT) is increasing in popularity due in part to its sustainable and biophilic effects [1,2]. CLT has been researched as a lateral load resisting system (LLRS) in platform construction where CLT shear walls are most commonly connected to floor panels above and below with standard connectors [3,4]. These standard connectors were adopted from light timber frame (LTF) construction and often have capacities of 100 kN or less if ductile performance under seismic loading is required [5,6]. LTF [7] or post-and-beam timber structures [8,9] are commonly employed for timber residential buildings which mainly use mechanical fasteners to connect timber members. LTF shear walls as lateral load resisting systems (LLRS) often use plywood or Oriented Strand Board sheathing with nailed panel-frame connections [10].

While LTF structures are commonly employed in Australasia for residential homes, CLT structures are well suited for multi-storey residential buildings with regular floor plans and an abundance of walls to use as LLRS. CLT LLRS could have limited strength and stiffness due to their performance being governed by small connectors [11]. For taller buildings or those with a limited amount of walls, high performance connections could meet increased strength and stiffness requirements [12,13], and also re-centering capabilities [14]. Another option could be to use vertical post-tensioning to replace standard commercial connectors which could maximize the stiffness achievable in a timber structure, minimize damage, and have strong re-centering capability, thus leading to a lower level of residual/permanent deformations/drifts [15,16].

Post-tensioned (PT) timber technology, also called Pres-Lam (Prestressed Laminated Timber), has been developed and tested at the University of Canterbury since 2005 [17]. The moment capacity at the wall base or beam-column joint is provided by the clamping action of the vertical unbonded post-tensioning tendons and/or in combination with special ductile energy dissipating devices which can either be internal and epoxied or external and replaceable [18]. To date, there are – to the best of the authors' knowledge - 13 Pres-Lam buildings constructed around the world and a state-of-the-art in research and implementation of this low-damage technology has been reported by Granello et al. [19]. Initial Pres-Lam development at the University of Canterbury focussed on laminated veneer lumber (LVL) due to its superior strength and stiffness properties when stressed parallel to grain in comparison to other mass timber products such as CLT. Nonetheless, CLT is a global product and more commonly implemented as a shear wall with exponential growth forecasted [20].

Extensive experimental testing has been performed on PT LVL single wall (SW) and hybrid single wall systems comprising special replaceable and ductile energy dissipating devices [17,18,21]. In order to provide increased energy dissipation, coupled double wall (DW) systems have been tested with U-shaped Flexural Plates (UFPs) [22] and nailed plywood in-plane joints to provide energy dissipation [23,24].

More recently, the Pres-Lam wall system has been tested using CLT [25–27], glulam [28–30] as well as systems with mixed materials, such as concrete-timber and steel-timber [31,32]. Under the multi-year Natural Hazards Engineering Research Infrastructure (NHERI) research project [33], PT CLT SW and DW systems have been tested under quasi-static and dynamic loading [26,34]. Further testing has also verified the performance of PT CLT SW and DW systems with and without axial or UFP dissipating elements [35,36]. In the previous PT DW testing, the in-plane joint has been utilized for its relative movement to dissipate energy. However, if strong and stiff connections with self-tapping screws (STS) are utilized, increased system strength and stiffness could be achieved with partial composite action of the wall panels.

STS are the most popular fasteners used in mass timber construction [37]. Work by Loss et al. [38] showed that the spatial insertion angle of the STS to the timber grain and loading direction significantly affects the performance. When installed at 90° to the loading direction, STS behave in dowel action with relatively lower strength and stiffness but relatively larger displacement and energy dissipation capability. When STS are installed inclined to the loading direction, they behave primarily in withdrawal action having relatively higher strength and stiffness, but lower displacement and energy dissipation capacity. By implementing mixed angle STS connections, high strength, stiffness and energy dissipative connections can be achieved [39–41]. For PT DW systems, STS installed at 90° with plywood at the in-plane joint could provide increased system strength and stiffness while also providing energy dissipation.

The behaviour of PT timber wall systems can be evaluated with the iterative moment-rotation analysis initially proposed by Pampanin et al. [42] for precast concrete, extended by Palermo [43] to capture the elastic range (called the Modified Monolithic Beam Analogy (MMBA)) and adopted by Newcombe et al. [44] for timber. In the MMBA procedure, some distinct characteristics of timber need to be considered, namely, the timber 'end effect' and timber compressive toe strain profile. Material testing of LVL identified a suitable strain limit and a stiffness reduction factor to account for the 'end effect', which accounts for the local end crushing of the timber fibres thus reducing the elastic modulus and axial stiffness of the timber section [45]. Further, in PT LVL SW testing, the compressive toe strain profile was investigated with a discrete number of Linear Variable Displacement Transducers (LVDTs) and strain gauges. The triangular and linear strain profile was deemed suitable for a low-damage design approach [46]. Due to the distinct material differences between LVL and CLT, the stiffness reduction factor and assumption of a linear stress/strain profile within the timber elastic range should be verified for CLT. Further, in order to better capture and monitor the compressive toe displacement and strain fields during the experimental tests on PT CLT walls, Particle Tracking Technology (PTT) [47] was implemented at the wall base. The MMBA analytical prediction model will be discussed in more detail in Section 5. The lateral behaviour of PT timber wall systems has also been characterized by defining a series of limit states with assumed stress strain profiles [48].

Currently, analytical prediction models for PT DW systems consider the kinematic rocking mode when both walls are in contact with the foundation, and assume a constant coupling force distribution (with elastoplastic or similar behaviour) along the in-plane joint [23,24,48]. This model was able to adequately capture the moment-rotation response when a relatively low coupling force due to nail or UFP yielding occurred [23,24] allowing for the two walls to develop a rocking motion at their base and a relative displacement at the yielding coupling devices. Gavric et al. [49] presented experimental testing and analytical prediction models for conventional CLT shear walls with commercial connectors and STS at the in-plane joint. The research reported that if a relatively large number of STS were installed, the wall acted as a combined single-coupled wall (SCW) with a single base rocking interface and kinematic mechanism. The model assumed a simplified trilinear load-displacement curve for all connections which makes it susceptible to sudden load-drops when the STS connection stiffness changes.

The combined single-coupled wall (SCW) kinematic rocking mode could also occur in PT DW systems depending on the relative strength and stiffness of the in-plane joint and the PT and dissipative elements. Because the STS force-displacement response is highly nonlinear with gradually changing stiffness, either the elastoplastic or the trilinear model for PT DW systems under the SCW kinematic mode might not be appropriate. The nonlinear curve fitting connection model presented by Foschi [50] could more accurately capture the PT DW system behaviour. Nonlinear curve fitting models are commonly implemented to capture the nail slip response in LTF construction types [10,51].

The primary objective of this experimental and analytical study is to assess the structural performance of PT single and double CLT shear wall systems coupled with STS at the in-plane joint and to provide comparison to a PT CLT shear wall with supplemental UFP dissipating devices. With increased in-plane joint strength and stiffness, partial composite action in the wall will increase and affect the kinematic rocking mode. Through Particle Tracking Technology the compressive toe behaviour of the PT CLT wall systems will be investigated to inform analytical prediction models. The secondary objectives are to extend the existing iterative MMBA analytical model for PT CLT wall systems as the model was originally developed for PT LVL walls. Finally, a proposed analytical model for PT DW systems primarily connected with STS will be validated with the experimental testing results.

## 2 TEST SPECIMEN DETAILING

The three phase PT CLT wall testing programme had a total of 17 tests under quasi-static cyclic loading, consisting of four PT Single Wall (SW) tests (Phase I), five PT Double Wall (DW) tests (Phase II), and eight PT and conventional core-wall testing (Phase III). The PT SW and DW specimens were tested with uni-directional testing protocol and the PT core-wall specimens were tested with either uni-directional and/or bi-directional testing protocol. This paper reports the experimental testing of Phase I and II and an overview of the key specimen detailing is provided. Further specimen detailing in Phase III PT core-wall testing can be found in Brown et al. [52]. A full description three Phase CLT shear wall testing programme can be found in Brown [53].

### 2.1 Wall Section Detailing

The CLT wall specimens were four-storeys high with a 2:3 scale factor. This scale factor was chosen due to lab restraints for the maximum CLT wall height, which then reduced the length of each wall in a similar manner. However, the CLT layup chosen (CLT wall thickness) was a readily available product size from the New Zealand CLT supplier. The walls were 8.6 m high and the individual walls were 1.912 m in length. The CLT panels were five-ply and 175 mm thick (45/20/45/20/45), with visually graded SG8 grade Douglas-Fir laminations as specified in NZS3603 - Timber Structures Standard [54]. The (unbonded) post-tensioning bars were located within 100 mm x 45 mm ducts in the middle layer of the CLT wall panels. The spacing of the post-tensioning bars was symmetrical about the in-plane joint for the DW specimens. Figure 1 shows the DW specimen cross section view with the coupling Wall 1 and Wall 2. During SW testing, only Wall 1 was present.

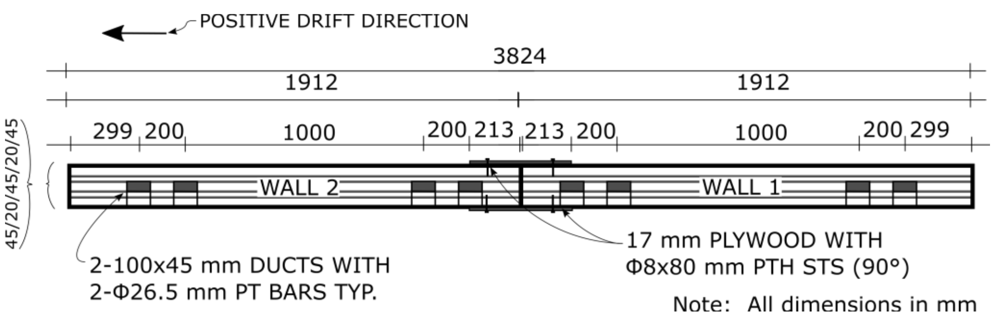


*Figure 1: Double wall cross section view*

## 2.2 Connection Detailing

### 2.2.1 Screwed Connections

As shown in Figure 1, the in-plane joint employed $\phi$8x80 mm partially threaded (PTH) STS installed at 90° to the CLT panel with 17 mm thick plywood as per NZS 3603 [54]. All STS were installed without predrilling following the minimum spacing ($a_1$=10d) as per Eurocode 5 [55] and the STS supplier European Technical Approval (ETA) [56]. The number of STS installed were 64, 220, and 64 for tests DW-2, DW-3 and DW-4 respectively as specified in Table 1 and the characteristic connection strength per STS was 3.3 kN as per Eurocode 5 [55]. 64 STS were used in Test DW-2 in order to provide similar re-centring ratio $\beta$ as Test DW-4 with UFPs and 220 STS were used in Test DW-4 based on preliminary calculations in order to achieve the combined single-coupled wall kinematic mode which will be described in Section 5.2.

### 2.2.2 Post-tensioning Bar and Anchorage

Figure 2 shows the post-tensioning bar location and anchorage detailing at the top of the CLT wall and the bottom with the steel foundation. A 500 mm long x 50 mm thick steel anchorage plate was used to spread the load from a pair of $\phi$26.5 mm high strength bars [57] at the top of the CLT wall. The Modulus of Elasticity and yield strength of the post-tensioning bars were 170 GPa and 835 MPa respectively. Side plates were welded to the 50 mm steel anchorage plate to provide confinement and restrict potential bulging effect of CLT under high axial loads. The shear keys at the wall base also provided confinement to the compression toe which is described further in Section 3.

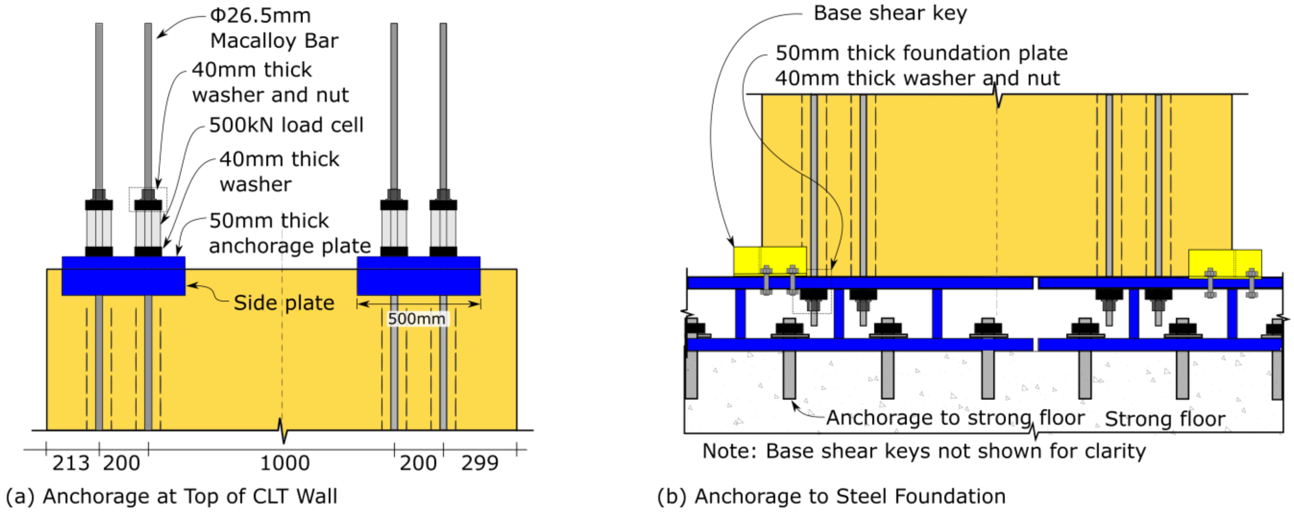


*Figure 2: Post-tensioning anchorage detailing at the wall base and top connections*

### 2.2.3 UFP Detailing

Pairs of mild steel U-shaped flexural plates (UFPs) [22,58] were located at the corners of each wall base as shown in Figure 3a. The mild steel Modulus of Elasticity and yield strength were 200 GPa and 300 MPa respectively. Figure 3b shows how each UFP pair was connected to the CLT wall. Each UFP was connected by 2-M16 bolts to a 12 mm thick steel plate, which was then connected to the face of the CLT wall with 8-$\phi$11x250 mm fully threaded STS [59] installed inclined at 45°. Each inclined STS connection was designed to remain elastic with an overstrength factor of 1.8 considering only STS under tension and neglecting friction and STS under compression. The UFPs were then connected to a short steel parallel flange channel (PFC) with 2-M16 bolts. The base of the PFC was then anchored to the foundation with 2-M20 bolts. 2-$\phi$12 mm Grade 4.6 threaded rods [60] were installed to connect the PFC and the steel plate to eliminate the induced force couple because the UFPs were placed only on one side of the CLT wall as similarly detailed on the Lucas House building due to architectural restrictions [61].

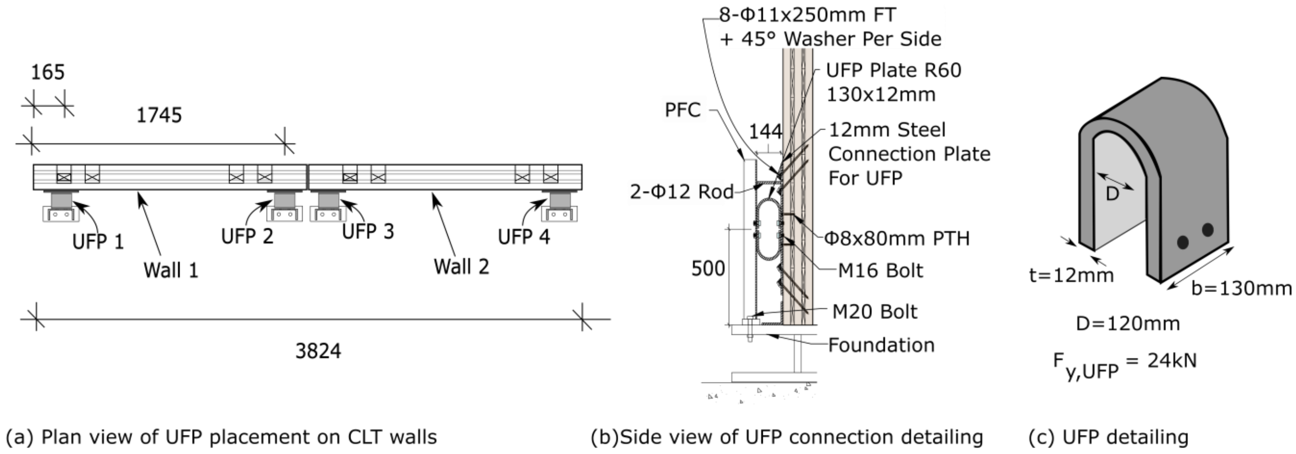


*Figure 3: UFP placement and connection detailing*

## 3 TESTING PROGRAMME AND METHODOLOGY

The testing programme for the PT SW and PT DW testing is provided in Table 1. In the PT SW testing, the initial post-tensioning bar force was varied. It was 0, 25, 50 and 75 kN/bar for the tests SW-1, SW-2, SW-3, and SW-4 respectively. The DW testing considered variations in terms of a) in-plane joint connection details; b) use of UFP dissipaters at the wall base; and c) re-centring ratio $\beta$, defined as $\beta = M_{pt}/M_{tot}$ where $M_{pt}$ is the base moment contribution due to PT bars and $M_{tot}$ is the total base moment capacity. In the DW testing, the initial post-tensioning force was limited to 5 % yield force of the PT bar to avoid potential yielding due to wall uplifting. Test DW-1 did not use STS or UFPs such that the frictional effect between the individual walls at the in-plane joint could be quantified. This also provided a baseline and lower bound DW performance. Tests DW-2 – DW-5 implemented STS at the in-plane joint, UFPs at the wall base, or both.

*Table 1: PT Single Wall (Phase I) and PT Double Wall (Phase II) testing programmes*

| **Test** | | **SW-1** | **SW-2** | **SW-3** | **SW-4** | |
|---|---|---|---|---|---|---|
| Initial PT / bar | kN | 0 (0%[1]) | 25 (5%[1]) | 50 (10%[1]) | 75 (15%[1]) | |
| **Test** | | **DW-1** | **DW-2** | **DW-3** | **DW-4** | **DW-5** |
| Initial PT / bar | kN | 25 (5%[1]) | 25 (5%[1]) | 25 (5%[1]) | 25 (5%[1]) | 25 (5%[1]) |
| In-plane Joint | Type | - | 8x80 PTH (17mm Ply.) | 8x80 PTH (17mm Ply.) | 8x80 PTH (17mm Ply.) | - |

| | | | | | | |
|---|---|---|---|---|---|---|
| | Qty. | - | 64 (90°) | 220 (90°) | 64 (90°) | - |
| UFPs | - | No | No | No | Yes | Yes |
| Re-centering Ratio ($\beta = M_{pt}/M_{tot}$) | - | 0.9 | 0.67 | 0.55 | 0.56 | 0.72 |

Note: [1] yield percentage of the post-tensioning bar; Qty. = quantity; PTH = partially threaded

The experimental test setup for the PT SW and the PT DW tests are shown in Figure 4. One 700 kN actuator with 4-M30 Grade 8.8 threaded rods was used to apply the lateral loads via a steel loading beam and bearing head at a wall height of 8.2 m. Two actuators provided out-of-plane restraints at 3.8 m and 7.4 m wall height for each wall. At the base of the wall, in-plane and out-of-plane translational restraints were provided by shear keys. The shear keys were equal angle 125 mm x 125 mm x 12 mm [62] with welds on the bottom leg only so that the top leg could yield and bend to accommodate the wall rocking as reported by Moroder et al. [27]. Such shear key details were also used for the Carterton Events Centre building [63]. The shear keys were bolted to the steel foundation beam with Grade 8.8 M20 bolts [62]. Each wall specimen had a capacity protected horizontal castellated joint at 5.5m wall height to transfer shear load through castellated joints and to resist overturning moments with steel straps connected to the wall above and below with STS (painted blue and shown in Figure 4). The horizontal joint was not a focus for Phase I (Single Wall) and Phase II (Double Wall) testing and further information can be found in Brown et al. [52] which reported Phase III (Core-wall) experimental results.

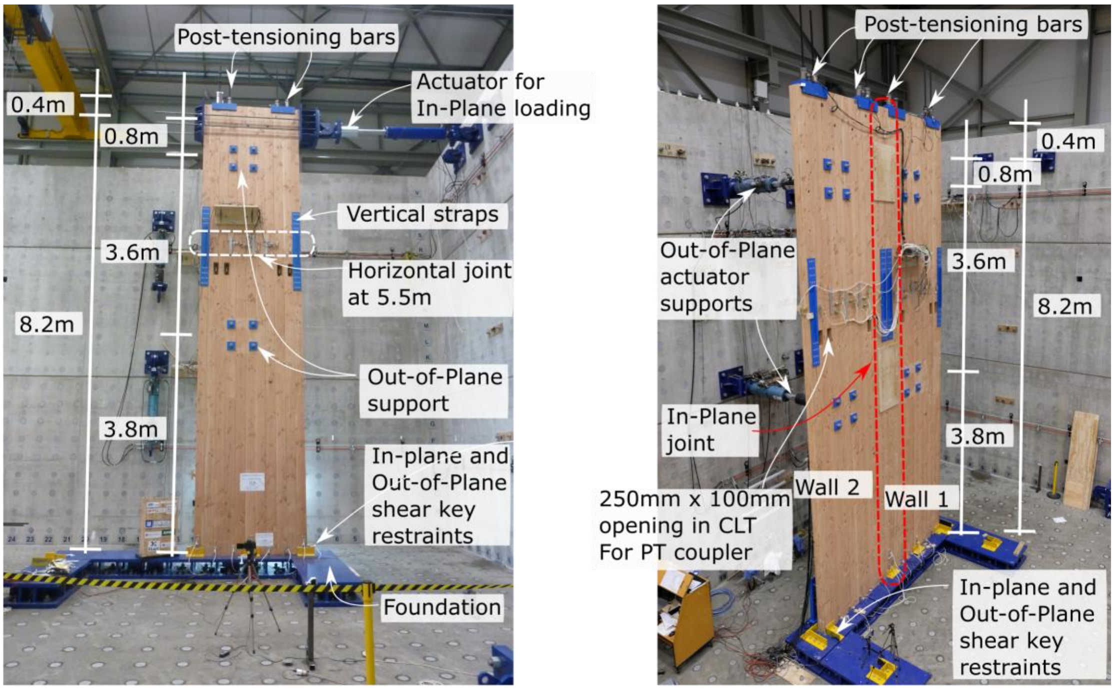


(a) Single Wall Test Set-Up (b) Double Wall Test Set-Up

*Figure 4: Single Wall (SW) and Double Wall (DW) Test Set-Ups*

The displacement controlled uni-directional loading protocol followed the ACI ITG-5.1-07 special protocol for PT precast structural walls [64]. The amplitude of each cycle group was 1.25 times that of the previous cycle group, and the first cycle group was 0.1 % drift as shown in Figure 5. Each cycle group had three identical cycles. The peak drifts were chosen during each test upon evaluation of the actual CLT compression strains and visible damage at the wall base.

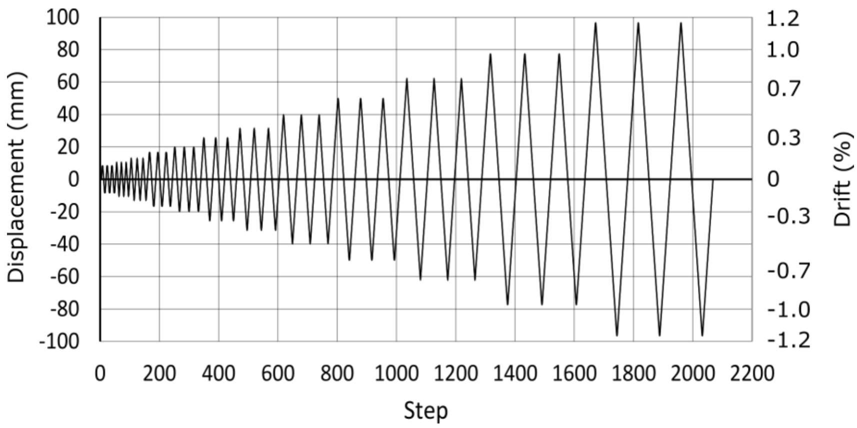


*Figure 5: Loading protocol*

## 3.1 Key Design Parameters and Instrumentation

The global responses of the walls were measured with linear variable differential transducers (LVDTs), load cells, and inclinometers. Specifically, Particle Tracking Technology (PTT) was implemented to measure the compressive toe strains at the wall base.

### 3.1.1 General Instrumentation

Figure 6 shows the key general instrumentation. LVDTs and inclinometers were placed on the specimen at 2m inter-storey heights to measure the wall joint relative slips, in-plane and out-of-plane deformations, and wall rotations. At the wall base, seven LVDTs measured the neutral axis depth (i.e., length of the compression zone) at the wall base and three LVDTs were placed on each UFP connection plate to measure vertical and horizontal movement. The actuators had 1000 kN load cells to monitor the applied load, and 500 kN load cells monitored the PT bar forces. As the PT bars were placed in pairs, the results of each bar were combined. LVDTs also tracked the movement of the steel foundation.

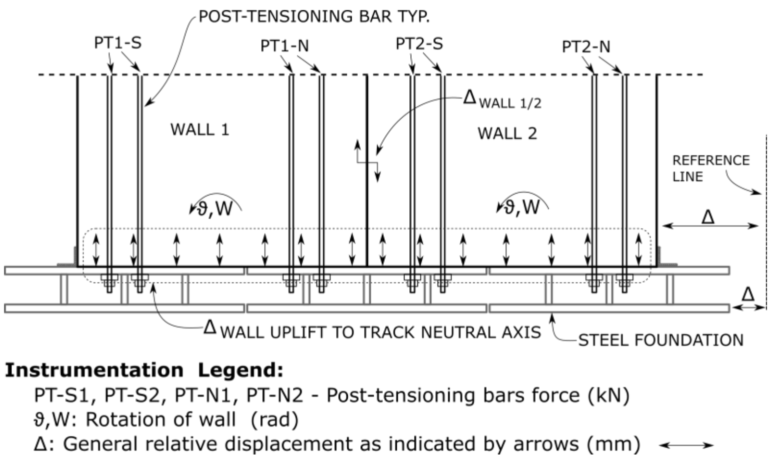


*Figure 6: Key instrumentation*

### 3.1.2 Particle Tracking Technology (PTT)

PTT was implemented at the base of each wall to track the base rocking interface. PTT is a contact-free quantitative field measuring technique originally developed to track individual particles in fluid flows [47].

More recently, Ottenhaus et al. [65] have shown . the versatility of PTT with CLT testing in dowel embedment tests, large scale CLT connection tests and small scale material tests to capture displacement and strain fields. Figure 7 shows the PTT setup and an image view of one camera tracking movement of the particles. The yellow painted shear keys interfered with the PTT data collection of the extreme fibre of the CLT compressive toe; however, the displacement and strain fields were captured above and beside the shear key which was deemed adequate. Six Fujifilm X-T2 cameras with XF 18-55 lens were positioned at the wall base on stiff supports. The resolution of the images was 6000x4000 pixels, and the PTT resolution ranged from 0.145 mm/pix to 0.197 mm/pix. Artificial lighting was provided to ensure a consistent light intensity throughout each image frame. 8 mm diameter blue or red circle stickers attached to the CLT wall surface were used as particles, and they were placed randomly on the timber surface for easier particle identification in post-processing. As the particles were placed on the timber face, all the measured displacement and strains represented the surface response. An image was captured at each displacement step of the loading protocol such that each image could easily be correlated with the associated experimental data file.

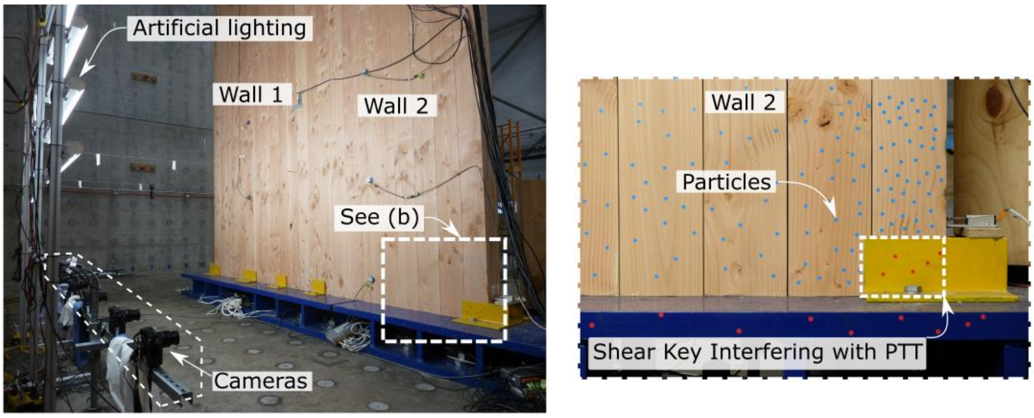


(a) Double wall PTT set-up

(b) Single camera view

*Figure 7: (a) PTT set-up and (b), single camera view*

*Streams* [47] was used in image post processing and it has an extensive toolkit of processes to perform image filtering, particle identification, PTT analysis, and ultimately produce displacement and strain fields. Within *Streams*, the pixels that comprise the particles are differentiated from the rest of the image frame by a variation in light intensity on either a grey or RGB scale. *Streams* generated a material displacement field on a rectangular grid corresponding to x, y, and t (the time of each image). Displacements were transformed into a material-based frame of reference such that displacements and strains were computed relative to the wall before testing began. Further details on PTT and implementation in the testing can be found in Brown et al. [66] and Ottenhaus et al. [65].

# 4 EXPERIMENTAL RESULTS AND DISCUSSION

The key experimental results are provided in Table 2. The results are provided at serviceability limit state (SLS, defined as 0.33 % inter-storey drift ratio) and a peak drift level. AS/NZS 1170.0 Appendix C [67] specifies SLS of 0.33 % for plaster/gypsum walls which are commonly used in NZ timber buildings. The peak drift level during the SW testing was limited to avoid plastic deformation greater than a few millimetres to the compressive toe, and for the DW testing, peak drift was limited to 1.2 % to avoid significant plastic deformation for the following Phase III core-wall testing [68]. While a peak drift of 1.2 % may be less than typical design building drifts, it was deemed sufficient to capture the major DW response which included the non-linear elastic behaviour due to gap opening at the wall base. The partial composite action (CA) in the DW can be defined by comparing the test results with a theoretical uncoupled and fully composite systems in a similar manner to that for composite beams [69] as:

$$\%\boldsymbol{CA_{\delta}} = \frac{\boldsymbol{F_{Test,\delta}} - \boldsymbol{F_{0\%,\delta}}}{\boldsymbol{F_{100\%,\delta}} - \boldsymbol{F_{0\%,\delta}}} \quad (1)$$

where, for a given wall drift ($\delta$), $F_{0\%,\delta}$ = the theoretical force for an uncoupled (non-composite) section; $F_{100\%,\delta}$ = the theoretical force for a fully composite section; and $F_{Test,\delta}$ = the measured force. Figure 8 shows the different rocking mechanisms such as a fully composite section, where there is no relative slip between two CLT walls, and a partial composite action where there is varying levels of relative displacement between the two walls. The theoretical calculations are based on a PT rocking wall boundary condition following the MMBA in accordance with the Pres-Lam design guide [70]. The MMBA procedure will be further described in Section 5. The total energy dissipation, $E_D$, was calculated as the area enclosed within the hysteresis loops for the entire loading protocol. The components of $E_D$ included friction between the CLT wall panels, yielding and embedment deformation of the screwed connections, and yielding of the UFPs which will be discussed further in Section 4.2.

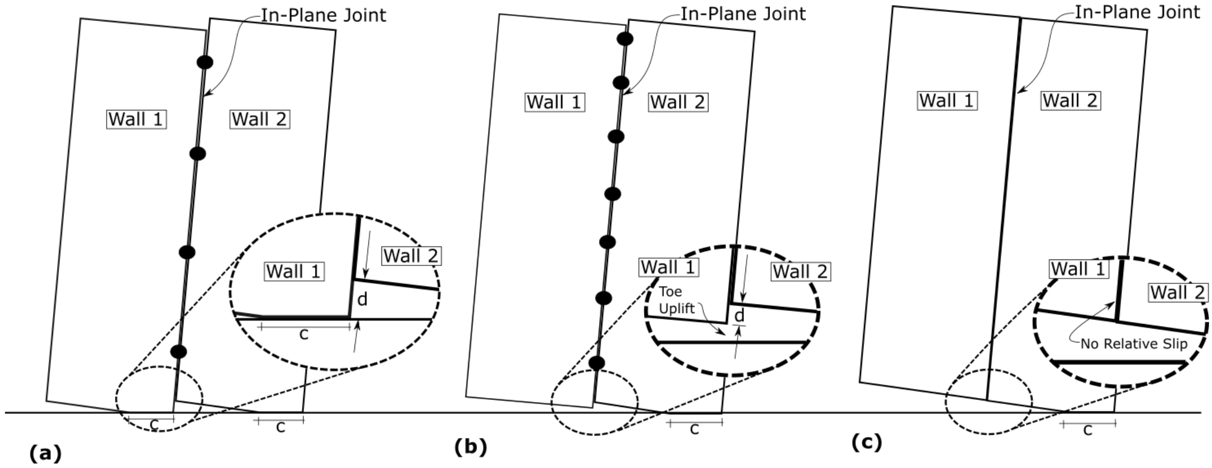


*Figure 8: Types of Double Wall Kinematics: (a) coupled double wall behaviour (partial composite action), (b) combined single-coupled wall behaviour (partial composite action), (c) theoretical single wall behaviour (100% composite action)*

## 4.1 Global Wall Response

For PT DW testing, Table 2 shows that the composite action decreased at the peak drift level when compared to the SLS. This was due to the gradual strength and stiffness degradation of the STS in-plane joint. The highest composite action of 70 % and 38 % at SLS and peak drift respectively was observed in Test DW-3. The low composite action in Test DW-1 indicated the friction contribution which had been noted previously by Moroder et al. [27]. The secant stiffness values at given drift levels include all possible slips and translational sliding due to the tolerances between the CLT wall panels. The SLS stiffness of 1.6 kN/mm achieved in Test DW-1 represents a lower bound for this PT DW system. The significant stiffness change in Tests DW-2, DW-3 and DW-4 indicated the impact of connection detailing on the system behaviour. In Test DW-3, the SLS stiffness was 3.7 kN/mm, more than two times of that achieved in Test DW-1, and almost four times of that achieved in Test SW-2 with the same initial post-tensioning. The yield percentage of the extreme PT bar, $\nu_{PT}$, is also reported in Table 2 and in Test DW-3, 40 % was reached at peak drift. The timber yield strain percentage, $\nu_T$, defined by the constitutive relation $E_0 = f_c/\varepsilon_T$, where $E_0$ is the timber Elastic modulus, $f_c$ is the compressive stress, and $\varepsilon_T$ is the compressive strain was determined by PTT.. This was unique when compared to past experimental testing by Sarti et al. [21], where timber strains were back calculated assuming a triangular distribution, or not quantitatively reported other than the test observations [26,35]. The compressive toe performance with PTT will be discussed in Section 4.3.

*Table 2: Wall testing experimental results summary*

| | Serviceability Limit State | | | | | Peak Drift | | | | | | |
|---|---|---|---|---|---|---|---|---|---|---|---|---|
| Test | CA (%) | F (kN) | k (kN/mm) | $\nu_{PT}$ (%) | $\nu_T$ (%) | Drift (%) | CA (%) | F (kN) | k (kN/mm) | $\nu_{PT}$ (%) | $\nu_T$ (%) | $E_D$ (kN-mm) |
| SW-1 | - | 16 | 0.6 | 7 | 26 | 1.2 | - | 53 | 0.6 | 30 | 66 | - |
| SW-2 | - | 29 | 1.1 | 14 | 29 | 0.93 | - | 57 | 0.7 | 31 | 69 | - |
| SW-3 | - | 32 | 1.2 | 17 | 37 | 0.93 | - | 63 | 0.8 | 33 | 64 | - |
| SW-4 | - | 38 | 1.4 | 23 | 32 | 0.75 | - | 64 | 1.1 | 34 | 64 | - |
| DW-1 | 11 | 45 | 1.6 | 13 | 22 | 1.2 | 9 | 124 | 1.3 | 36 | 66 | 17,040 |
| DW-2 | 34 | 66 | 2.4 | 13 | 25 | 1.2 | 19 | 155 | 1.6 | 37 | 79 | 38,680 |
| DW-3 | 70 | 100 | 3.7 | 17 | 21 | 1.2 | 38 | 217 | 2.3 | 40 | 61 | 65,300 |
| DW-4 | 39 | 71 | 2.6 | 13 | 6 | 1.2 | 23 | 169 | 1.8 | 36 | 70 | 41,420 |
| DW-5 | 16 | 49 | 1.8 | 12 | 10 | 1.2 | 15 | 144 | 1.5 | 35 | 37 | 22,090 |

Note: CA is composite action; $\nu_{PT}$ is the yield percentage of the extreme post-tensioning bar; $\nu_T$ is the yield strain percentage of the extreme timber fibre value, determined by PTT and assuming $E_0$ = 9,700 MPa and $f_c$ = 37 MPa as per as per component testing in Section 6.1.1; $E_D$ = total energy dissipation during full loading protocol

Figure 9 shows the plots for base shear versus drift, moment versus wall base rocking interface rotation (connection rotation), and neutral axis depth versus connection rotation for the four PT SW tests. A typical non-linear elastic behaviour due to the gap opening at the wall base was observed. Increased initial post-tensioning forces delayed the onset of gap opening, and then the post gap opening wall stiffness was similar for all the tests as expected. The neutral axis depth ratio (c/L), where c is the length of the compression zone and L is the wall length (1.912 m)) was approximately 0.15 and slightly increased with increased initial post-tensioning forces. The minimum c/ L ratio was also not exactly symmetrical due to the slightly non-symmetrical placement of the PT bars as shown in Figure 1. Further, additional force occurred on the positive “push” wall drift direction due to out-of-plane wall twist. This wall twist occurred primarily because there was only one pin-pin connection of the out-of-plane rams and also because the in-plane loading actuator could rotate due to its pin-pin connection (with spherical bearings) under compression. Because of this, all analytical comparisons in Section 6 are made to the negative “pull” wall drift cycles.

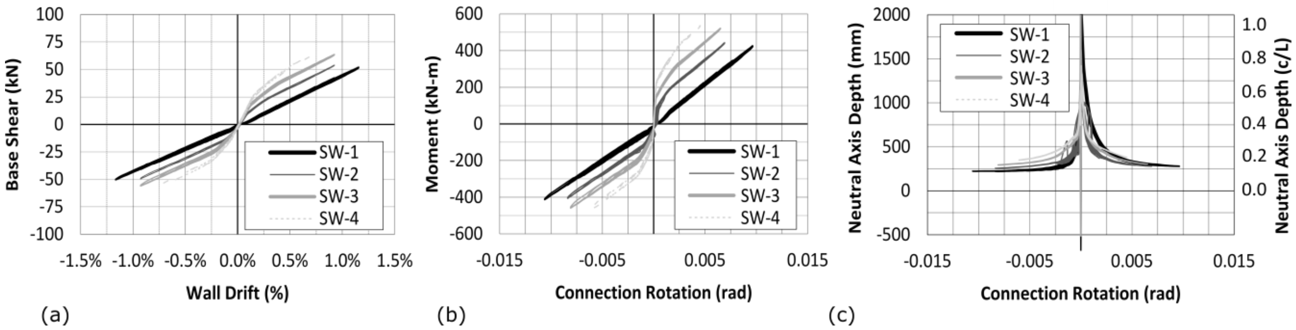


*Figure 9: SW test series summary: (a) base shear – drift; (b) moment – rotation; and (c) neutral axis depth – connection rotation*

Figure 10 shows the key plots for Tests DW-2, DW-3, and DW-4. The base shear vs wall drift curves are compared with the theoretical fully composite ($F_{100\%,\delta}$) and non-composite ($F_{0\%,\delta}$) PT walls. At low drift levels, Test DW-3 closely matched the theoretical fully composite curve. This was primarily due to the STS in-plane joint having high initial stiffness. However, with gradual stiffness degradation of the STS joint the DW systems gradually tended away from the theoretical upper bound. All post-tensioning forces are reported as a pair as described in Section 3. In Test DW-3, the increase in PT1-N forces during positive drift cycles indicated tendon elongation due to wall uplift which will be discussed in detail.

The neutral axis behaviour during each test was similar for Wall 1 and Wall 2 due to the symmetrical behaviour of the test setup. During Test DW-3, the neutral axis behaviour was significantly different as a negative neutral axis was reported which indicated one wall uplift. This unique behaviour has not been observed in past PT

DW testing that used the in-plane joint slip to provide increased energy dissipation during the rocking motion [23,24,26,35]. At a base connection rotation of approximately 0.006 rad, the wall touched the ground, and a positive neutral axis was reported. The neutral axis depth ratio (c/ L) was approximately 0.25 in Test DW-3, which was larger than Tests DW-2 and DW-4 where the c/L ratio was closer to 0.15 at peak drift. Residual drift was negligible in all tests except DW-3 where it was 0.1 %. The relative connection slip at the in-plane joint varied in each test due to the different strength and stiffness of the STS connection details and UFP devices. At 1.2 % wall drift, the connection slips were 17.1 mm, 15.1 mm, and 16.1 mm for Tests DW-2, DW-3, and DW-4, respectively.

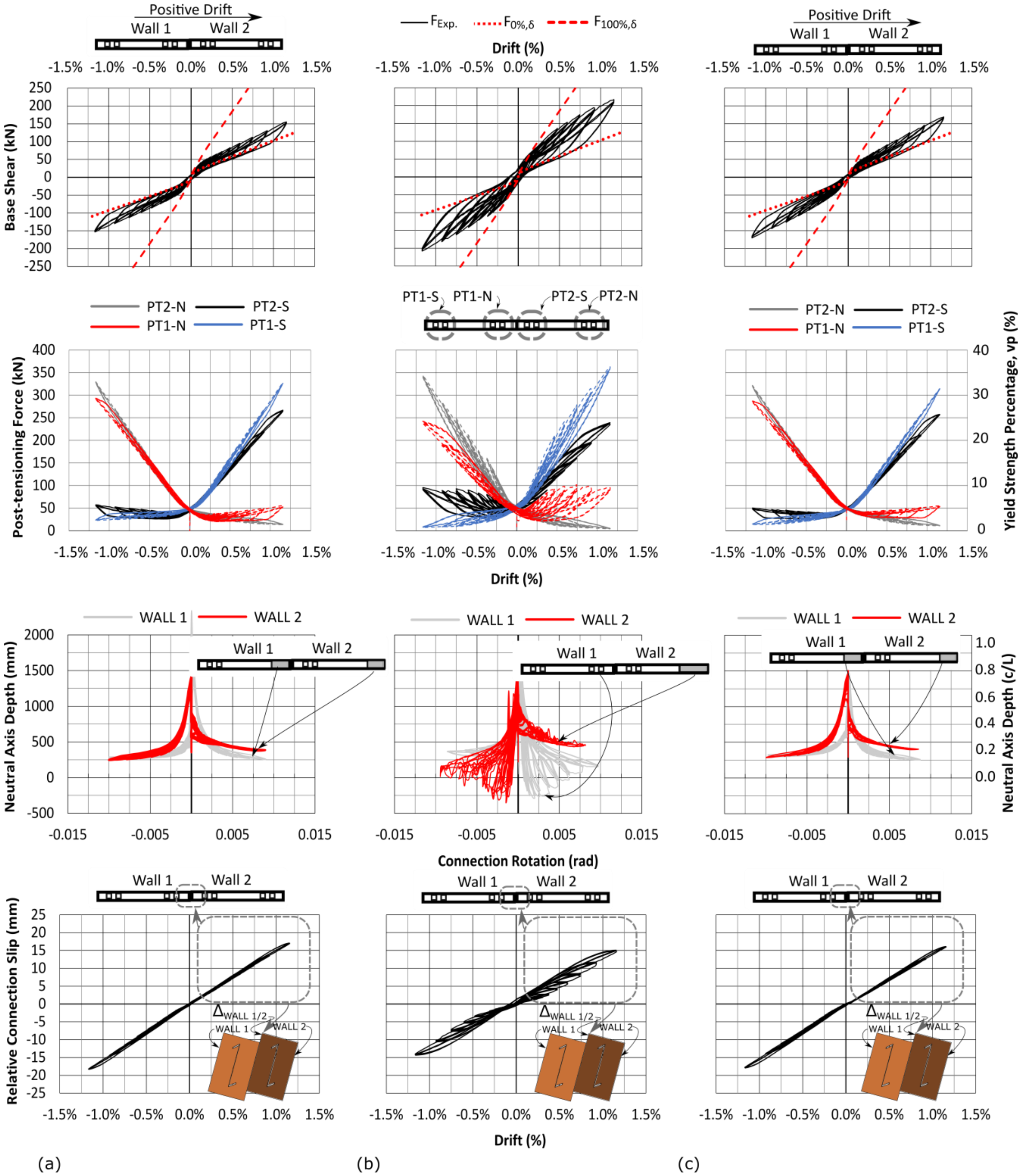


*Figure 10: DW testing Key Plots: (a) Test DW-2, (b) Test DW-3, (c) Test DW-4*

## 4.2 Connection Response

The UFPs and their connection detailing, STS connection at the in-plane joint, and compressive toe performance were evaluated. The 12 mm thick steel UFP connection plate (see Figure 3) had +0.6 mm in the +1.2 % cycle and -1.1 mm in the -1.2 % drift cycles while the UFPs had greater than 10 mm vertical displacement due to gap opening at the wall base. Residual displacement of the steel UFP connection plate was -0.3 mm which indicated that embedment deformation occurred in the inclined STS connection. Further, it was found that the UFPs were also able to undergo twisting and out-of-plane movement without fracture due to their placement in front of the walls instead of the wall ends. More details on UFP connection performance can be found in Brown et al. [68]. The STS connections performed differently when compared to other mild steel dissipaters generally employed for hybrid PT walls. The STS connections still provided stable global behaviour given the tested wall drifts but pinching of the hysteresis curves was observed which could reduce total energy dissipation. The pinching behaviour occurs physically due to the presence of gaps between the fastener and wood caused from plastic timber embedment deformation [10]. This phenomenon has also been reported by Iqbal et al. [71]. The performance difference between STS and mild steel could be observed by comparing the results between Test DW-2 (STS implemented) and Test DW-5 (UFPs implemented). While the $\beta$ ratio was comparable, Test DW-2 with STS dissipated 75 % more energy. This was primarily due to the fact that the UFPs required a relatively large imposed displacement prior to yielding due to lower stiffness; their rolling motion was not perfectly vertical; and small slips existed in their connections to the CLT panels and steel parallel flanged channel (PFC). It was found that an approximately 12 mm imposed displacement was required for the UFPs to reach their yielding plateau, determined by the UFP component testing results (see Section 6.1.2). This corresponded to approximately 0.8 % wall drift. In contrast, the STS connections reached yielding at approximately 5 mm connection displacement [72] and significant energy dissipation could occur at even lower imposed displacements. This 5mm in-plane joint displacement corresponded to approximately 0.25 % wall drift. It should be noted this comparison is limited to the wall drifts of 1.2 % when the STS joint displacement reached 15 mm. Work by Hossain [72] showed that peak load of this type of STS connection occurs at approximately 19 mm displacement (see Figure 19). Therefore, the displacement and energy dissipation capacity of a PT DW system with STS would be limited and significant strength and stiffness degradation would occur beyond 19 mm connection displacement. In contrast Baird et al. [58], for example, have shown that UFPs have stable performance at significantly larger deformations. The in-plane relative joint slip increased slightly with the increased wall height due to elastic deformation of the walls. However, the in-plane joint slip difference was less than 2 mm over the wall height. At 1.2 % wall drift, the relative slip was 15.1 mm and 16.2 mm at 0.4 m and 4 m wall height respectively.

### 4.3 Compressive Toe Performance

PTT was utilized to determine the strain field within each compressive toe region over the lower 260 mm wall height, along the entire compressive toe length. Figure 11 gives a summary of experimental testing strain results for Test SW-2 in comparison with the MMBA assumption at different drift levels. At each drift cycle, the scatter and the mean of timber strain are compared with the MMBA predictions (shown with grey lines) which assumed a triangular distribution, a timber elastic modulus as per **Error! Reference source not found.**, and $k_{gap}$ = 0.7 as per the Pres-Lam Design Guide [70]. The experimental neutral axis depth at each drift cycle is also shown on each graph with a solid red vertical line.

Further, at each drift cycle, and at each compressive toe, the peak average compressive strain was compared with the peak timber strain determined by the MMBA. A strain amplification factor $\phi_t$ defined as the ratio between the experimental strain and the MMBA analytical strain was determined. Table 3 summarizes the results of all SW tests for both the positive and negative drift cycles, and significant differences were observed. It was also found that a higher concentration of knots existed on the negative drift cycle side compared to the positive drift side of the wall base. This could cause generally different compressive strains between positive and negative cycles at the same drift. The average strain amplification factor $\phi_t$ was found to be 1.3, based on a total of 37 analytical to experimental comparisons over the four tests. It should be noted that the $\phi_t$ factor of 1.3 was determined based on a limited number of experimental tests. Future work is needed to investigate different wall configurations, drift demands, timber species and engineered timber products. Nonetheless, the variability in compressive strains over the 260 mm wall base height highlighted the inherent variability of timber and which could be higher when using non-edge glued visually graded dimensional lumber as lamella for the CLT. Based on the PTT results from Tests SW-1 to Test SW-4 (SW-2 shown in Figure 11), it seemed that a linear strain distribution was appropriate, based on the mean experimental strains presented (shown in black).

*Table 3: Summary of timber strain amplification factors*

| Test | Negative Drift | Positive Drift | Average |
|---|---|---|---|
| SW-1 | 2.0 | 1.9 | 2.1 |
| SW-2 | 2.1 | 1.0 | 1.4 |
| SW-3 | 1.4 | 1.5 | 1.4 |
| SW-4 | 1.7 | 0.7 | 0.9 |
| Average | 1.8 | 1.1 | **1.3** |

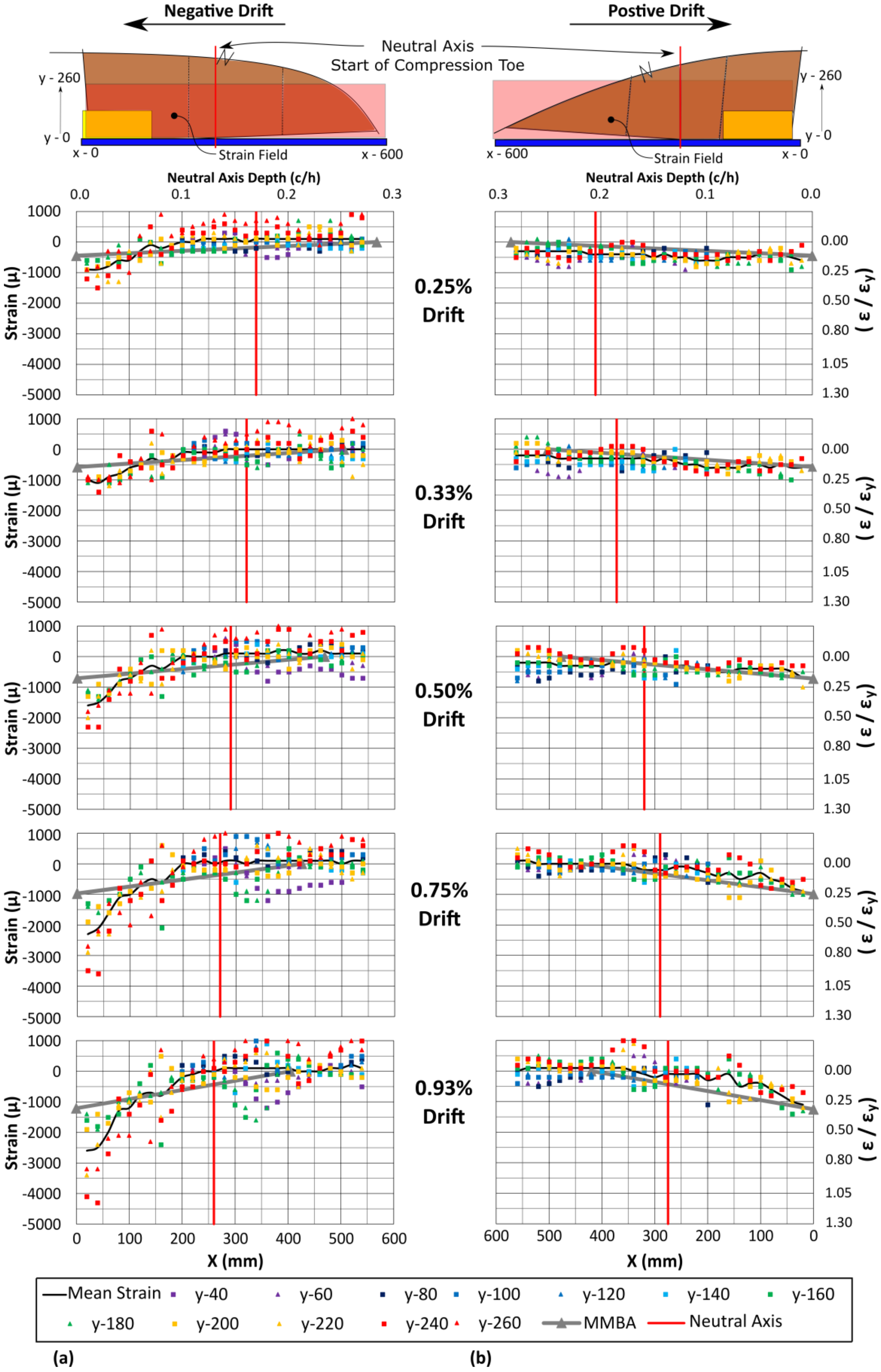


*Figure 11: Test SW-2 compressive toe strain comparison to MMBA*

# 5 ANALYTICAL MODELLING OF POST-TENSIONED SINGLE AND DOUBLE WALLS

The response of PT rocking timber walls can differentiated in two phases: before and after wall base gap opening. Before gap opening, the response can be modelled as a fixed base cantilever wall. With increasing initial post-tensioning force, the required overturning moment to initiate gap opening, called the decompression moment, will increase. The decompression moment, $M_{dec}$, to initiate gap opening is determined as:

$$\boldsymbol{M_{dec}} = \frac{\boldsymbol{Z}}{\boldsymbol{A_{eff}}}\left(\sum \boldsymbol{T_{PT,o}} + \boldsymbol{N}\right) \tag{2}$$

where Z = section modulus of the CLT wall cross-section which only considers the longitudinal CLT timber lamella; $A_{eff}$ = effective cross-sectional area of the CLT walls which only considers the longitudinal CLT timber lamella; $\sum T_{PT,o}$ = total initial post-tensioning force; and $N$ = axial force from gravity loading.

Once $M_{dec}$ is reached, gap opening and a wall base connection rotation, $\theta_j$, will occur. The total displacement, $\delta_T$, after gap opening at the top of a wall can be determined as:

$$\boldsymbol{\delta_T} = \boldsymbol{\delta_r} + \boldsymbol{\delta_b} + \boldsymbol{\delta_s} \tag{3}$$

where $\boldsymbol{\delta_r}$ = rocking deformation as discussed in Section 5.1 and 5.2; $\delta_b$ = elastic bending deformation as discussed in Section 5.3; $\delta_s$ = elastic shear deformation as discussed in Section 5.3.

## 5.1 Post-Tensioned Single Wall Rocking Deformation Theory

The rocking deformation, $\delta_r$, is determined for a given wall base connection rotation, $\theta_j$, as shown in Figure 12 as:

$$\boldsymbol{\delta_r} = \boldsymbol{\theta_j H_{cant}} \tag{4}$$

where $H_{cant}$ is the cantilever wall height.

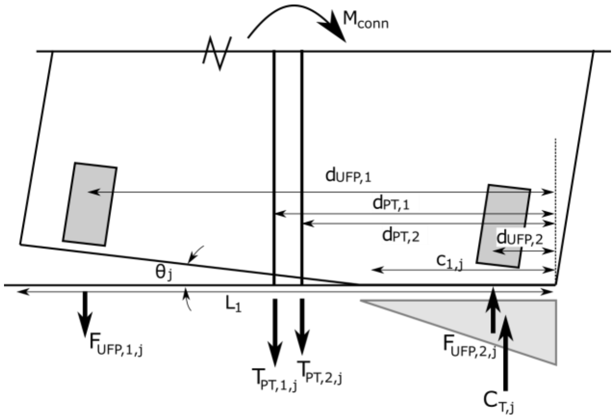


*Figure 12: PT Single Wall Sectional Analysis*

For an imposed wall base connection rotation, $\theta_j$, the tendon elongation is determined by geometry due to gap opening with consideration for axial wall shortening as:

$$\Delta_{\boldsymbol{PT,i,j}} = \boldsymbol{\theta_j}\left(\boldsymbol{d_{PT,i}} - \boldsymbol{c_{1,j}}\right) - \frac{\left(\sum \boldsymbol{T_{PT,j}} - \sum \boldsymbol{T_{PT,o}}\right)\boldsymbol{l_{ub,i}}}{\boldsymbol{E_o A_{eff}}} \tag{5}$$

where $\Delta_{PT,i,j}$ = elongation of the i-th post-tensioning bar for the j-th rotation increment; $d_{PT,i}$= edge distance of the i-th post-tensioning bar (See Figure 12); $c_{1,j}$ = neutral axis depth for the j-th rotation increment; $\sum T_{PT,j}$ = sum of post-tensioning bar force for the j-th rotation increment; $l_{ub,i}$ = unbonded length of the i-th post-tensioning bar; $E_o$ = timber elastic modulus. $T_{PT,i,j}$ can then be evaluated as:

$$\boldsymbol{T_{PT,i,j}} = \boldsymbol{T_{PT,i,0}} + \frac{\Delta_{\boldsymbol{PT,i,j}}}{\boldsymbol{l_{ub,i}}}\boldsymbol{E_{PT} A_{PT,i}} \tag{6}$$

where $E_{PT}$ = post-tensioning steel bar elastic modulus; $A_{PT,i}$ = cross-section area of the i-th post-tensioning bar. For UFP devices placed at the wall base, the imposed displacement is found in a similar manner as the PT bars:

$$\Delta_{\boldsymbol{UFP,i,j}} = \boldsymbol{\theta_j}\left(\boldsymbol{d_{UFP,i}} - \boldsymbol{c_{1,j}}\right) \tag{7}$$

where $\Delta_{UFP,i,j}$ = elongation of the i-th UFP element for the j-th rotation increment; and $d_{UFP,i}$ = edge distance of the i-th UFP element (see Figure 12); and $c_{1,j}$ = neutral axis depth for the j-th rotation increment. Experimental tests by Skinner et al. [73] and then by Baird et al. [58] have shown the force-displacement behaviour of UFP devices can be modelled by a Ramberg-Osgood function [74] as shown in Figure 14b. Then, the timber compressive force, $C_{T,j}$ (see Figure 12), is evaluated according to a member strain compatibility condition outlined with the MMBA [44] procedure which assumes that the displacement of a rocking element is analogous to a monolithic element. Herein, it is suggested that the strain amplification factor, $\phi_t = 1.3$, is included when considering the non-edge glued CLT.

$$\boldsymbol{C_{T,j} = 0.5 E_{con} b_{eff} c_{1,j}^2 \left(\frac{3\theta_j}{H_{cant}} + \frac{M_{dec}}{E_{con} I_{eff}}\right) \phi_t} \tag{8}$$

where $E_{con}$ = timber connection modulus = $k_{gap}E_o$; $b_{eff}$ = sum of CLT longitudinal board widths; $I_{eff}$ = second moment of inertia which considers $b_{eff}$. $k_{gap}$ within $E_{con}$ accounts for the reduction in axial stiffness, thus reducing $E_o$, due to the ‘end effect’ as discussed by Newcombe et al. [44] for LVL and presented in Section 6.1.1 for the CLT tested herein. Finally, the force equilibrium as per Eq. **9** is assessed and if not satisfied, the neutral axis depth $c_{1,j}$ is iterated until the equilibrium is achieved.

$$\boldsymbol{C_{T,i,j} - \sum T_{PT,i,j} - \sum F_{UFP,i,j} = 0} \tag{9}$$

Then, the base connection moment for a wall base connection rotation, $\theta_j$, can be evaluated as:

$$\boldsymbol{M_{conn,j} = \sum T_{PT,i,j}\left(d_{PT,i} - {c_{1,j}}/{3}\right) + \sum F_{UFP,i,j}\left(d_{UFP,i} - {c_{1,j}}/{3}\right)} \tag{10}$$

Then, the elastic bending and shear deformations are determined as per Section 5.3 in order to determine the total wall deformation as per Eq. **3**.

## 5.2 Post-Tensioned Double Wall Rocking Deformation Theory

As shown in Figure 8, the PT DW rocking deformation can be separated into three different kinematic modes: coupled double wall (CDW) behaviour, combined single-coupled wall (SCW) behaviour, and theoretical single wall behaviour. These kinematic modes were originally suggested for CLT shear walls by Gavric et al. [49]. In a PT DW system, the in-plane joint provides the coupling force. Depending on the relative strength and stiffness of the in-plane joint to the PT bars and the dissipative elements, a certain kinematic behaviour will occur. Thus, after evaluating the dissipative device forces, an additional step which evaluates the coupling force at the in-plane joint must be added. With the STS in-plane joint, this coupling force changes nonlinearly depending on the relative joint slip. For each given wall base connection rotation, $\theta_j$, the relative joint slip, $d_{2,j}$ must be evaluated as well.

### 5.2.1 Coupled Double Wall (CDW) Theory

In the CDW kinematic behaviour, both Wall 1 and Wall 2 are in contact with the foundation, as shown in Figure 13.

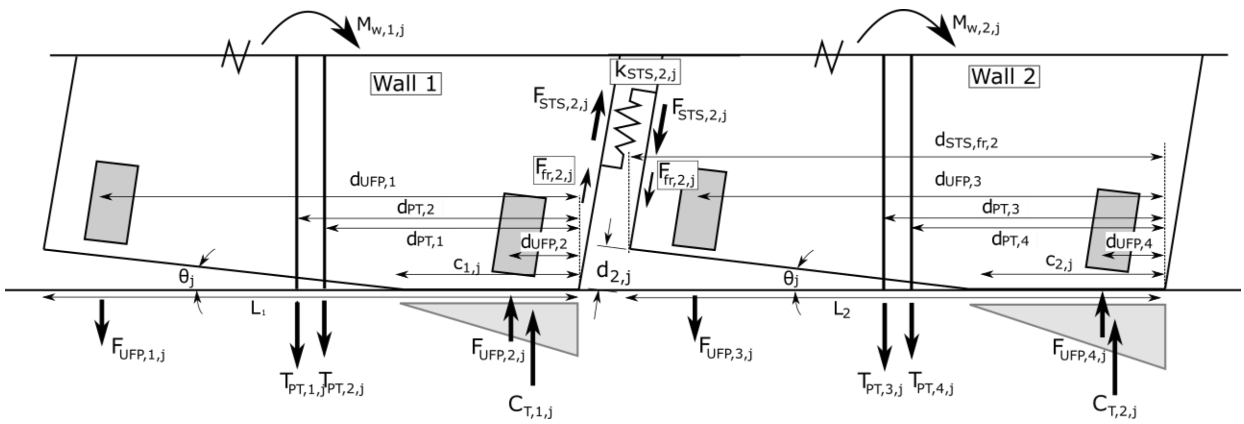


*Figure 13: Section analysis of post-tensioned double wall with UFPs and STS connectors under kinematic coupled double wall behaviour mode*

In order to evaluate the coupling force at the in-plane joint, the relative displacement, $d_{2,j}$, between the wall panels at the base is required and is approximated as:

$$\boldsymbol{d_{2,j} = \theta_j \cdot (L_2 - c_{2,j}) + \theta_j \cdot c_{1,j}} \tag{11}$$

where $c_{i,j}$ = neutral axis length for wall *i* for the j-th rotation increment; and $L_2$ = length of Wall 2. Considering elastic deformations of the wall panels, the relative displacement will increase along the height of the in-plane joint. However, based on the test results presented in Section 4 and the fact that the rocking deformation is significantly greater than the elastic deformation, it is thus assumed $d_{2,j}$ is uniform along the entire in-plane joint in the analytical model. The compressive displacement in Wall 1 ($\theta_j \cdot c_{1,j}$) is approximated and it will be compared to experimental results. The coupling force provided by the STS joint, $F_{STS,2,j}$ can be determined as:

$$\boldsymbol{F_{STS,2,j} = n_{STS,2} k_{STS,2,j} d_{2,j} = K_{STS,2,j} d_{2,j}} \tag{12}$$

where $n_{STS,2}$ = the number of STS pairs along the in-plane joint; $k_{STS,2,j}$ = the stiffness of a STS pair for a given displacement, $d_{2,j}$; $K_{STS,2,j}$ = the total stiffness of the in-plane joint for a given displacement, $d_{2,j}$. The load-displacement behaviour of laterally loaded STS, similar to any dowel-type fastener in timber, is highly non-linear. In order to accurately capture the nonlinear behaviour, numerous past research [10,51] has used an exponential function. In this research, the model originally proposed by Foschi [50,75] to capture the envelope curve (OAI in Figure 14a) was implemented as shown in Equations 13 - 15.

$$\boldsymbol{F_{STS,2,j} = sgn(d_{2,j})(F_o + r_1 K_o |d_{2,j}|)(1 - exp\left(-\frac{K_o |d_{2,j}|}{F_o}\right)), |d_{2,j}| \leq |d_{2,u}|} \tag{13}$$

$$F_{STS,2,j} = sgn(\boldsymbol{d_{2,j}})(F_{STS,2,u} + r_2 K_o)(\boldsymbol{d_{2,j}} - sgn(\boldsymbol{d_{2,j}}) d_{2,u}), |d_{2,u}| < |\boldsymbol{d_{2,j}}| \leq |d_{2,f}| \tag{14}$$

$$F_{STS,2,j} = 0, |d_{\boldsymbol{2,j}}| > |d_{2,f}| \tag{15}$$

where $F_{STS,2,j}$ = connector force as per Foschi model; $sgn(d_{2,j})$ = signum function to extract the sign of the displacement, $d_{2,j}$; $d_{2,u}$ = displacement at maximum force; $d_{2,f}$ = final displacement. Figure 14 shows the cyclic load-displacement models of a dowel-type fastener (STS) by Foschi [50,75] and a UFP by means of the Ramberg-Osgood function [58,74]. While past research [23,26,34,35] and built examples such as the NMIT Arts and Media Building [76] have utilized UFPs, dowel-type fasteners can also provide and energy dissipation through yielding of the fastener and plastic timber embedment deformation [10,71].

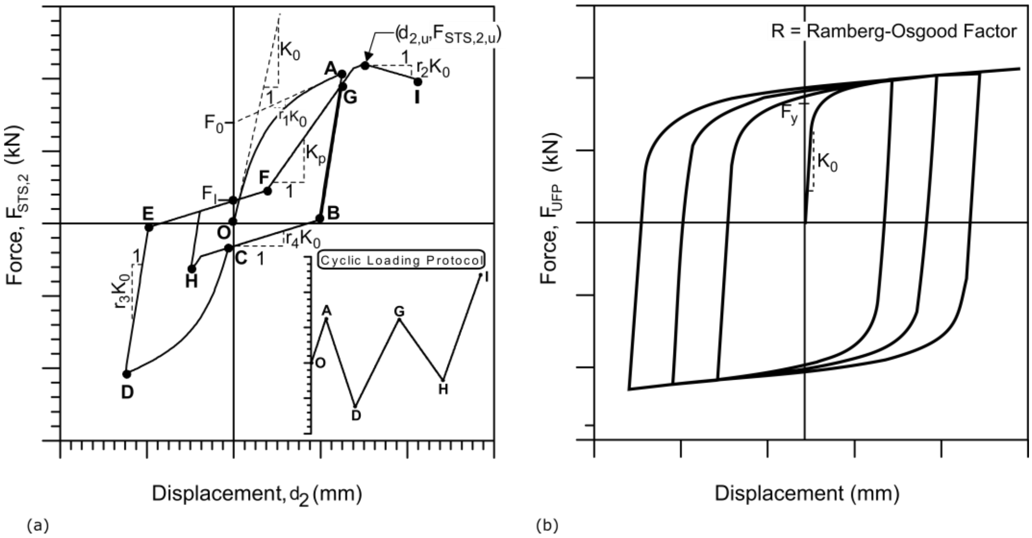


*Figure 14: (a) Nail-slip model proposed by Foschi* [50] *with figure from Folz & Filiatrault* [51]*, (b) UFP force displacement model by means of the Ramberg-Osgood function* [74]

Gavric et al. [49] and Iqbal et al. [24] proposed simplified trilinear and bilinear load-displacement curve fitting models respectively to account for the coupling force between CLT panels with dowel-type fasteners. In Section 6.3, Test DW-2 will be compared to the analytical model using the simplified bilinear elastoplastic curve fitting model as proposed by Iqbal et al. [24].

With reference to Figure 13, the equilibrium for Wall 1 and Wall 2 is determined as:

$$\boldsymbol{C_{T,1,j} + F_{fr,2,j} + F_{STS,2,j} + F_{UFP,2,j} - \sum T_{PT,i,j} - F_{UFP,1,j} = 0} \tag{16}$$

$$C_{T,2,j} - F_{fr,2,j} - F_{STS,2,j} - F_{UFP,3,j} - \sum T_{PT,i,j} + F_{UFP,4,j} = 0 \tag{17}$$

The neutral axis depth, $c_{1,j}$ and $c_{2,j}$, is then iterated until force equilibrium is achieved. Note, the friction term is generally neglected [77,78] in analysing CLT structures. In this study it is considered as it was required to predict the experimental response under quasi-static loading where friction was present. The friction co-efficient was calibrated based on Test DW-1 and kept constant for the remaining double wall tests. Once equilibrium is achieved the base connection moment can be determined for Wall 1 and Wall 2 with reference to Figure 13 as:

$$\boldsymbol{M_{w,1,j}} = \sum \boldsymbol{T_{PT,i,j}} \left(\boldsymbol{d_{PT,i}} - {}^{\boldsymbol{c_{1,j}}}/_{\boldsymbol{3}}\right) + \boldsymbol{F_{fr,2,j}} \left({}^{\boldsymbol{c_{1,j}}}/_{\boldsymbol{3}}\right) + \boldsymbol{F_{STS,2,j}} \left({}^{\boldsymbol{c_{1,j}}}/_{\boldsymbol{3}}\right) + \sum \boldsymbol{F_{UFP,i,j}} \left(\boldsymbol{d_{UFP,i}} - {}^{\boldsymbol{c_{1,j}}}/_{\boldsymbol{3}}\right) \tag{18}$$

$$\begin{aligned} M_{w,2,j} = {} & \sum T_{PT,i,j} \left(d_{PT,i} - {}^{c_{2,j}}/_{3}\right) + F_{fr,2,j} \left(d_{fr,2} - {}^{c_{2,j}}/_{3}\right) + F_{STS,2,j} \left(d_{STS,2} - {}^{c_{2,j}}/_{3}\right) \\ & + \sum F_{UFP,i,j} \left(d_{UFP,i} - {}^{c_{2,j}}/_{3}\right) \end{aligned} \tag{19}$$

The friction and STS coupling forces can be assumed to be acting along the in-plane joint line. In reality, the STS will be placed with a minimum edge distance (3d = 24mm) from the panel edge but this small difference was neglected for simplification. The total base connection moment, $M_{conn,j}$, is then:

$$\boldsymbol{M_{conn,j}} = \boldsymbol{M_{w,1,j}} + \boldsymbol{M_{w,2,j}} \tag{20}$$

Then, the elastic bending and shear deformations are determined as per Section 5.3 and Eq. **3**.

### 5.2.2 Combined Single-Coupled Wall (SCW) Theory

In the SCW kinematic behaviour, the coupling force and stiffness is large enough such that Wall 1 is not in contact with the ground, as shown Figure 15. However, there is a relative slip, $d_{2,j}$, between Wall 1 and Wall 2 which is less than the uplift of Wall 2 at the in-plane joint.

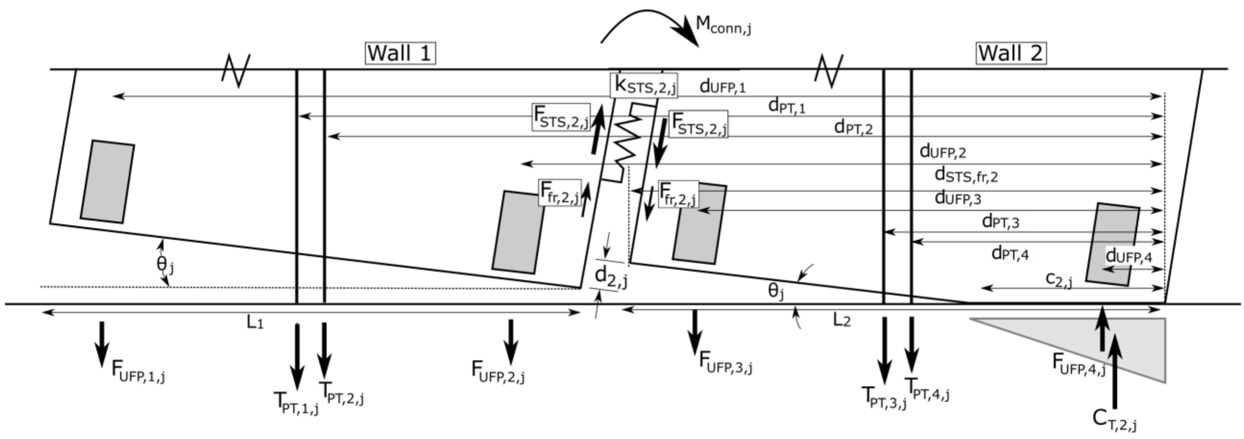


*Figure 15: Section analysis of post-tensioned double wall with UFPs and STS connectors under kinematic combined single-coupled wall behaviour mode*

In order to determine $d_{2,j}$, the vertical force equilibrium of Wall 1 is determined considering the stiffness and deformation of each post-tensioning and dissipative element:

$$\sum \boldsymbol{k_{PT,i,j}}[(\boldsymbol{d_{PT,i}} - \boldsymbol{c_{2,j}})\boldsymbol{\theta_j} - \boldsymbol{d_{2,j}}] + \sum \boldsymbol{k_{UFP,i,j}}[(\boldsymbol{d_{UFP,i}} - \boldsymbol{c_{2,j}})\boldsymbol{\theta_j} - \boldsymbol{d_{2,j}}] + \sum \boldsymbol{T_{PT,0,w1}} = \boldsymbol{K_{STS,2,j}}\boldsymbol{d_{2,j}} + \boldsymbol{F_{fr,2,j}} \tag{21}$$

where $k_{PT,i,j}$ = stiffness of the 'i-th' PT bar for the 'j'-th rotation increment; $k_{UFP,i,j}$ = stiffness of the 'i-th' UFP element for the 'j'-th rotation increment. With reference to Figure 15, vertical force equilibrium of the two wall system can be determined as:

$$\boldsymbol{C_{T,2,j}} - \sum \boldsymbol{T_{PT,i,j}} - \boldsymbol{F_{UFP,1,j}} - \boldsymbol{F_{UFP,2,j}} - \boldsymbol{F_{UFP,3,j}} + \boldsymbol{F_{UFP,4,j}} = \boldsymbol{0} \tag{22}$$

The post-tensioning bar and dissipater forces can be determined as per Section 5.1 considering the relative wall slip, $d_{2,j}$. By rearranging Equation **21**, an expression for the relative slip between two walls can be determined for a given wall base connection rotation, $\theta_j$, and Wall 2 neutral axis depth, $c_{2,j}$.

$$\boldsymbol{d_{2,j}} = \frac{\boldsymbol{\theta_j}\{\sum \boldsymbol{k_{PT,i,j}}[(\boldsymbol{d_{PT,i}} - \boldsymbol{c_{2,j}})] + \sum \boldsymbol{k_{UFP,i,j-1}}[(\boldsymbol{d_{UFP,i}} - \boldsymbol{c_{2,j}})]\} - \boldsymbol{F_{fr,2,j}} + \sum \boldsymbol{T_{PT,0,w1}}}{(\boldsymbol{K_{STS,2,j-1}} + \sum \boldsymbol{k_{PT,i,j}} + \sum \boldsymbol{k_{UFP,i,j-1}})} \tag{23}$$

Again, the friction component $F_{fr,2,j}$ can be neglected in design but is included here for comparison to the quasi-static experimental testing results. Equation **23** shows that as $K_{STS,2,j}$ decreases the relative connection slip, $d_{2,j}$, increases. The base connection moment, $M_{conn,j}$, can be evaluated as:

$$\boldsymbol{M_{conn,j}} = \sum \boldsymbol{T_{PT,i,j}}\left(\boldsymbol{d_{PT,i}} - {}^{\boldsymbol{c_{2,j}}}/_{\boldsymbol{3}}\right) + \sum \boldsymbol{F_{UFP,i,j}}\left(\boldsymbol{d_{UFP,i}} - {}^{\boldsymbol{c_{2,j}}}/_{\boldsymbol{3}}\right) \tag{24}$$

The SCW kinematic behaviour continues until Wall 1 toe touches the foundation, which is when $d_{2,j} = \theta_j \cdot (L_2 - c_{2,j})$. Once this occurs, the kinematic behaviour changes to CDW as described previously in Section 5.2.1. Then, the elastic bending and shear deformations can be determined as per Sections 5.3.

### 5.3 Elastic Deformations of Walls

The bending deformation, $\delta_b$, at the top of the wall is calculated using the elastic bending deflection formula for a fixed base cantilever beam as:

$$\boldsymbol{\delta_{b,j}} = \frac{\boldsymbol{F_j H_{cant}^3}}{\boldsymbol{3 E_o I_{eff,\gamma}}} \tag{25}$$

where $F_j$ = the horiztonal force at the top of the wall for a given wall base rotation 'j'; and $E_o I_{eff,\gamma}$ = the effective flexural stiffness of the CLT panel by considering the longitudinal layer only [79]. For coupled walls with composite action, the 'gamma method' in Eurocode 5 [55] was used to calculate the effective flexural stiffness.

There are different methods in literature for calculating the in-plane shear deformation, $\delta_{s,j}$, of a CLT panel [80]. In this instance, the shear stiffness method proposed by Schickhofer et al. [81] was used which determines an effective shear modulus, $G_{eff}$, and the gross shear area, $A$ as:

$$\boldsymbol{G_{eff} A} = \frac{\boldsymbol{G_0 A}}{\boldsymbol{1 + 6\left[0.32\left(\frac{t_b}{a}\right)^{-0.77}\right]\left(\frac{t_b}{a}\right)^2}} \tag{26}$$

where $t_b$ = average thickness of the CLT lamella; $a$ = the average width of the CLT lamella. Then, the shear deformation for a given wall base rotation 'j' is determined as:

$$\boldsymbol{\delta_{s,j}} = \frac{\boldsymbol{F_j H_{cant}}}{\boldsymbol{G_{eff} A}} \tag{27}$$

# 6 ANALYTICAL-EXPERIMENTAL COMPARISONS

## 6.1 Material Properties and Input Parameters

The analytical models described in Section 5 require the timber modulus of elasticity parallel to grain, $E_0$, timber 'end-effect' factor, $k_{gap}$, UFP and post-tensioning bar properties, and the STS connection properties. These properties can be determined from design codes, supplier information, and the Pres-Lam design guide [70] or through material property testing. In order to verify the proposed analytical models, material property testing were undertaken.

### 6.1.1 CLT Compression Tests for End-Effect Calibration

Compression testing as per EN 408 [82] was employed to assess the CLT properties. Figure 16 shows the test setup for the CLT5 and CLT3 specimens which implemented Particle Tracking Technology. The cross-section dimensions for the compression tests were 100 mm x 175 mm x 600 mm high for CLT5 (5-layer) specimens and 70 mm x 60 mm x 360 mm for CLT3 (3-layer) specimens. Past work by Newcombe et al. [44] with LVL showed that the axial stiffness of a timber section is not constant throughout the specimen length due to the 'end-effect'. To account for the 'end effect' of timber under crushing loads, a reduced stiffness should be used following the adjustment factor, $k_{gap}$. For LVL $k_{gap}$ = 0.7 was recommended for design [70]. Figure 16c shows the CLT5 stress-strain curve when the 'end effect' is considered (shown in grey) and when a gauge length is used (shown in black). The number of replicates for each CLT layup was five and the mean values are reported with coefficient of variation in parenthesis in Table 4. For the CLT5 specimen, the $k_{gap}$ factor was 0.83 and for the CLT3 specimens, the $k_{gap}$ factor was 0.71.

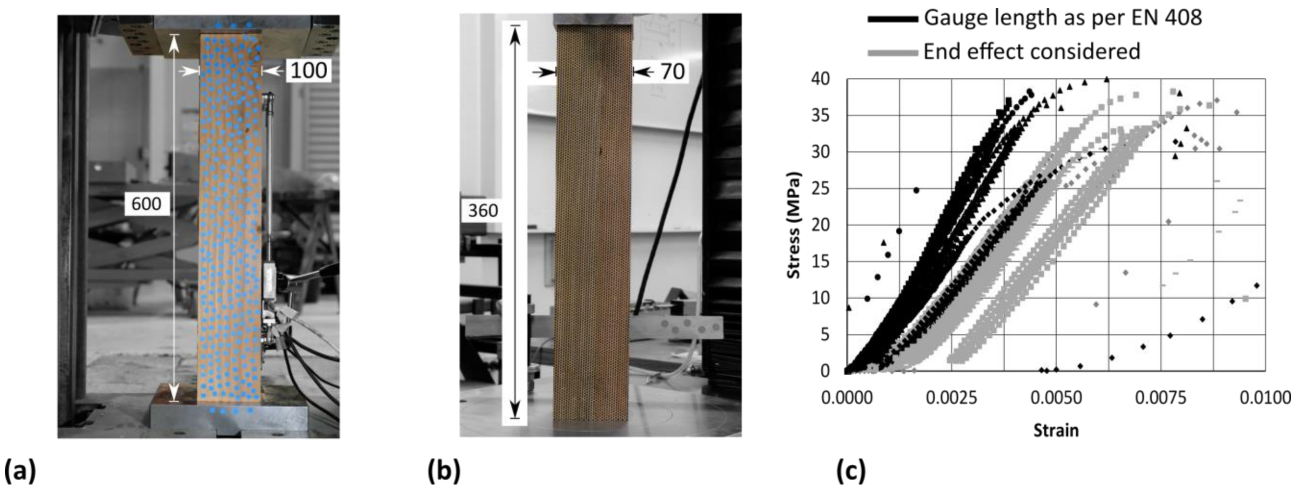


*Figure 16: CLT compression testing: (a) CLT5 test set-up, (b) CLT3 test set-up, and (c) CLT5 experimental results*

*Table 4: CLT Compression Testing Results*

| Layer thickness | $E_{0-End}$ | $E_o$ | $k_{gap}$ | $f_c$ |
|---|---|---|---|---|
| | MPa | MPa | | MPa |
| 45mm | 8,028 (4%) | 9,707 (13%) | 0.83 | 37 (9%) |

| | | | | |
|---|---|---|---|---|
| 20mm | 9,489 (4%) | 13,435 (6%) | 0.71 | 54 (7%) |
| SG8 NZS 3603 [54] | - | 8,000 | 0.7[1] | 18 |

Note:[1] $k_{gap}$ = 0.7 is as per Post-Tesnioned Timber Buildings Design Guide (Pampanin et al., 2013)

### 6.1.2 Testing of UFPs

The UFPs were tested separately to evaluate their cyclic performance. They were fabricated from 12 mm thick Grade 300E [83] steel plates and bent to the specified dimensions. The UFPs had a 60 mm inner radius, and a width of 130 mm. The test set-up and the force-displacement curves are shown in Figure 17. The maximum force for the UFP pair was much larger than the analytical plastic capacity of 46 kN based on the steel yield strength of 300 MPa. However, this is within the overstrength of 145 % - 215 % found by Kelly et al. [22] compared with the yield strength obtained from direct tension tests and further explained in Baird et al. [58]. Figure 17b shows no significant difference between Tests 1 and 2 with the unused UFP pairs and Test 3 which tested used UFPs from location UFP1 of Figure 3 on the PT DW specimen. Overall, the performance of the UFPs between the three tests was very consistent. The elastoplastic curve fitting parameters were $F_{UFP}$ = 71 kN and $k_{ufp}$ = 5.5 kN/mm for a pair of UFPs as shown in Figure 17b.

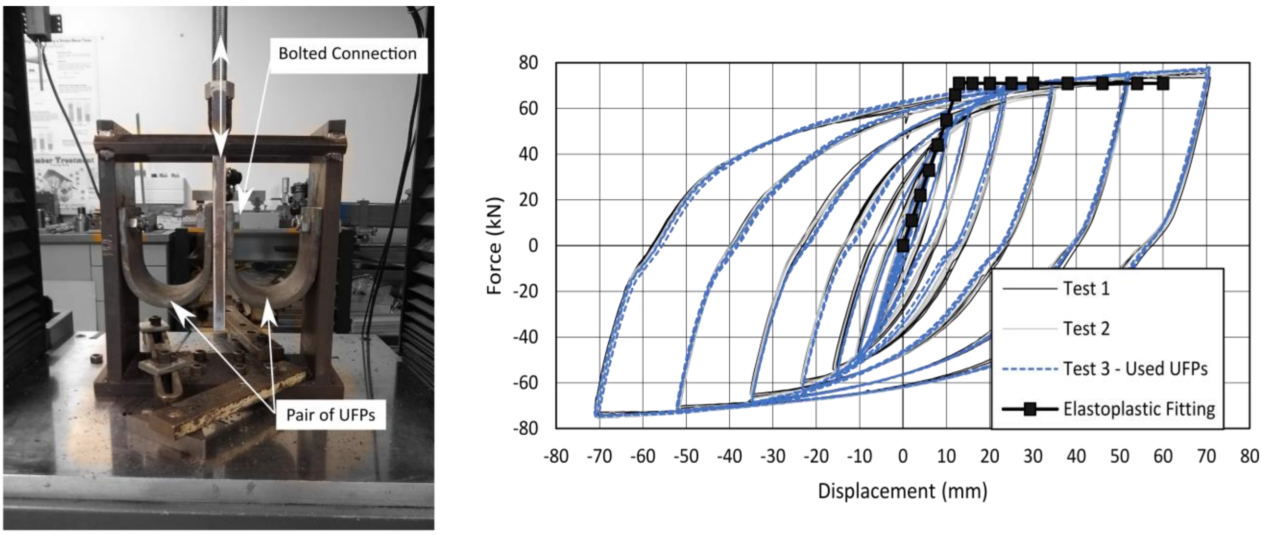


(a) (b)

*Figure 17: UFP component testing: (a) test setup; and (b) UFP component testing force-displacement curves*

### 6.1.3 Testing of Post-Tensioning Bars

The post-tensioning bars were tested to verify their material properties. The tensile tests were performed on three replicates of machined coupons using a 1000 kN Avery test machine and followed the loading protocol as per BS EN ISO 6892-1 [84]. Figure 18 provides details of the machined specimen, test set-up and experimental results. The specimens were processed following BS EN ISO 6892-1 [84] to determine the 0.1 % and 0.2 % proof stresses. The elastic modulus, $E_{PT}$, was determined by fitting a line to the linear portion of the stress-strain curve. The specimens were not tested to tensile failure in order to avoid damage to the test equipment. Once a load drop was observed at the onset of necking, the specimen was unloaded and its behaviour was recorded. The results showed mean $E_{PT}$ = 184 GPa, 8 % greater than the provided $E_{PT}$ = 170 GPa [57].

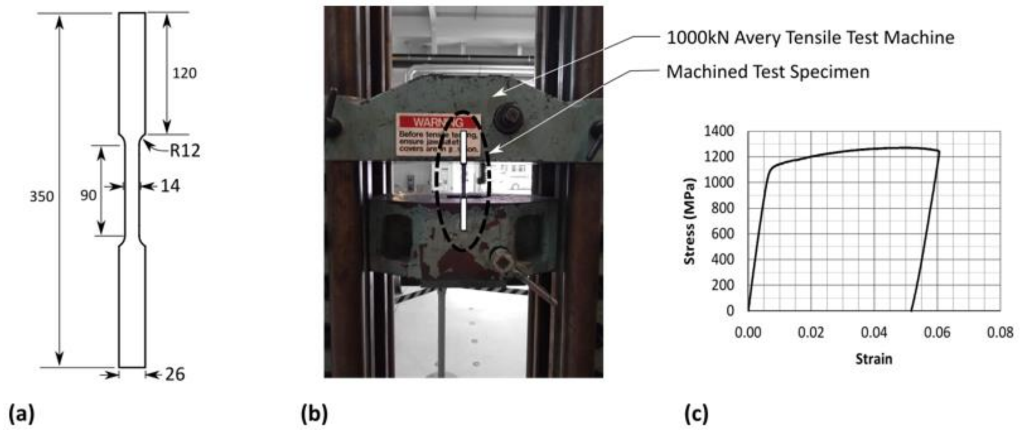


*Figure 18: Post-tensioning bar machined specimen, test setup, and results*

### 6.1.4 STS In-Plane Joint

STS component connection tests were not performed in this study as sufficent test data by Hossain [72] was available. Figure 19 shows the connection load-slip curves by Hossain [72], the comparison between the experimental curve, the fitted exponential curve following the Foschi model [50], and the fitted curve by the simplified elastoplastic method as assumed by Iqbal et al. [24]. Table 5 lists the curve fitting parameters required to fit the envelope curve OAI shown in Figure 19b. The elastoplastic curve fitting parameters were $F_{STS}$ = 4.8 kN/STS and $k_{STS}$ = 0.6 kN/mm for a pair of STS UFPs as shown in Figure 19b.

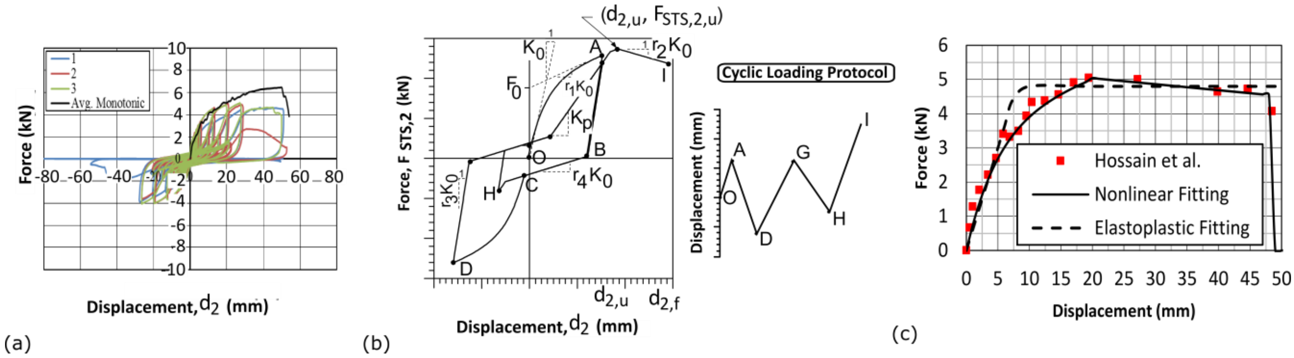


*Figure 19: (a) STS component testing by Hossain* [72], *(b) nonlinear curve fitting model by Foschi* [50], *(c) curve fitting results*

*Table 5: Input parameters for non-linear curve fitting model*

| Initial Stiffness | Force Intercept | Stiffness reduction parameters | | Displacement at max. force | Displacement at final displacement | Max. force |
|---|---|---|---|---|---|---|
| (kN/mm) | (kN) | | | (mm) | (mm) | (kN) |
| $K_0$ | $F_0$ | $r_1$ | $r_2$ | $d_{2,u}$ | $d_{2,f}$ | $F_{STS,2,u}$ |
| 0.8 | 3.81 | 0.08 | -0.022 | 19.41 | 48.47 | 5.05 |

The number of STS pairs installed in Test DW-2, DW-3, and DW-4 was 32, 110, and 32 respectively which then amplified the curve fitting shown in Figure 19c for a single STS pair as per Equation 12.

## 6.2 Single Wall Testing Comparison

Figure 20 compares experimental Test SW-2 to the analytical model using the different input parameters of the wall components. Due to the out-of-plane twisting of the specimen on the positive 'push' cycle as discussed in Section 4, the comparison was only made to the negative 'pull' drift cycles. When the readily available material properties were used, including timber graded SG8, post-tensioning bar properties as per ETA [57], and $k_{gap}$ = 0 .7 as per Pres-Lam design guide [70], the moment-rotation behaviour was predicted within 15%. These readily available material values were obtained from the NZS 3603 – Timber Structures Standard [54] and NZS 3404 – Steel Structures Standard [60], product brochures and design guides. When the material component testing data were used, i.e., $E_o$ = 9700 MPa, $k_{gap}$ = 0.83, and $E_{PT}$ = 184 GPa as per Section 6.1, the analytical prediction error of the moment rotation was within 10 %. Finally, when the material component properties and the strain amplification factor $\phi_t$ were applied, the analytical prediction error of the moment rotation was within 5 %. Further, the neutral axis prediction was closer to the experimental results, which then corresponded to a well-predicted post-tensioning bar behaviour and better prediction of the peak timber strain. The neutral axis was still slightly over predicted; however, it was acknowledged that there could be errors in how the neutral axis is determined based on data processing of experimental results with LVDTs. Work by Kovacs [85] showed that there is error associated with linearly interpolating the results between a discrete number of LVDTs. This is in part due to the fact that there is a curvature formed at the wall base and the fact that there is a slope change in the displacement when part of a wall shifts from uplifting to contacting the ground. Refer to Brown et al. [66] for further discussion on the compression toe performance.

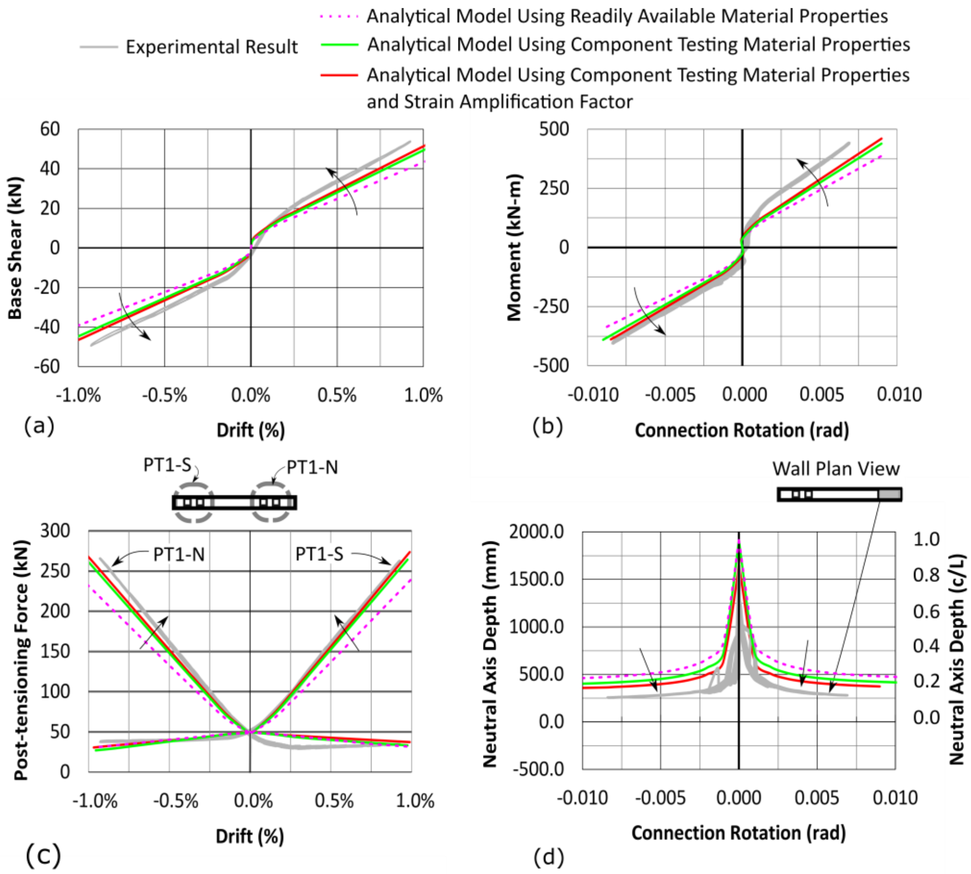


*Figure 20: SW-2 Comparison to analytical model with different input material properties*

## 6.3 Double Wall Testing Comparison

A summary of experimental-analytical comparisons of Wall 2 kinematics is presented in Table 6 as a percentage of total deformation. On average, the wall kinematics was predicted within 10 % error for all the tests with different levels of coupling. The material component testing data presented in Section 6.1 and $\phi_t$ were used in all experimental-analytical comparisons. With Test DW-1, the coefficient of friction was found to be $\psi$ = 0.30 which was within the range found by past research [86]. The frictional force between Wall 1 and Wall 2 was calculated by $F_{fr} = \psi F$, where $F$ was the ram force. Note, the friction term is generally neglected [77,78] in deflection calculation and modelling of CLT structures but this was presented for comparison to the experimental quasi-static testing results.

*Table 6: Post-tensioned double wall, Wall 2 experimental-analytical kinematics comparison*

| | | Experimental | | | Analytical | | |
|---|---|---|---|---|---|---|---|
| | Loading Direction | $\delta_r$ | $\delta_{sl}$ | $\delta_b + \delta_s$ | $\delta_r$ | $\delta_{sl}$ | $\delta_b + \delta_s$ |
| Test | | (%) | (%) | (%) | (%) | (%) | (%) |
| DW-1 | Positive | 82 | 3 | 15 | 80 | 0 | 20 |
| | Negative | - | - | - | 80 | 0 | 20 |
| DW-2 | Positive | 77 | 2 | 21 | 72 | 0 | 28 |
| | Negative | 86 | 2 | 12 | 78 | 0 | 22 |
| DW-3 | Positive | 70 | 5 | 25 | 61 | 0 | 39 |
| | Negative | 81 | 5 | 14 | 75 | 0 | 25 |
| DW-4 | Positive | 74 | 1 | 25 | 67 | 0 | 33 |
| | Negative | 85 | 2 | 15 | 75 | 0 | 25 |
| DW-5 | Positive | 77 | 1 | 22 | 76 | 0 | 24 |
| | Negative | 86 | 1 | 13 | 77 | 0 | 23 |

Note: $\delta_{sl}$=wall drift due to base sliding.

Figure 21 compares Test DW-2 to the coupled double wall (CDW) analytical model using both the elastoplastic and the nonlinear curve fitting model for the in-plane STS joint. At low wall drifts (less than 0.25 %), the system strength and stiffness were slightly under predicted which could in part be due to the increased friction at the onset of rocking motion as described by Moroder et al. [27]. However, at increased drifts there is good agreement. Figure 21b shows that under the CDW kinematic mode, the simplified elastoplastic curve fitting approach implemented by Iqbal et al. [24] was sufficient to capture the moment-rotation response.

Figure 22 compares Test DW-3 to the analytical model. During the testing, wall uplift defined within the single-coupled wall (SCW) kinematic behaviour was observed until the 0.93 % drift cycle when the SCW mode changed to the CDW mode. The red solid line curve is the SCW kinematic behaviour and the red dashed curve represents the CDW kinematic behaviour. The CDW behaviour was triggered when Wall 1 toe touched the foundation, as shown in Figure 22f. The non-linear curve fitting model by Foschi [50] was able to capture the gradually degrading stiffness of the in-plane joint with increased connection slip. In the PT DW systems with high composite action, the simplified elastoplastic curve fitting approach for the STS connection however seemed not appropriate. The analytical model captured the force-drift and moment-rotation curve within 10% error at each drift level (see Figure 22a-b). Further, the “negative” neutral axis, which signified wall uplift, was captured reasonably well with the model (see Figure 22d). The connection slip was slightly underestimated in the model (Figure 22e) and the increased experimental relative slip could be due to the large number of loading cycles that were performed at lower drifts whereas the STS component data from Hossain et al. [72] implemented a different loading protocol. Wall 1 toe uplift was captured well (with slightly lower uplift values) as shown in Figure 22f. When the analytical toe uplift prediction intersected 0 at 0.004 rad, Wall 1 was in contact with the ground. This was also reflected by the neutral axis curve in Figure 22d. The ‘gamma factor’ as per Eurocode 5 [55] used to calculate the effective flexural stiffness was found to be 10 % at SLS drift and then less than 2 % at peak drift due to the gradually degrading stiffness of the in-plane joint.

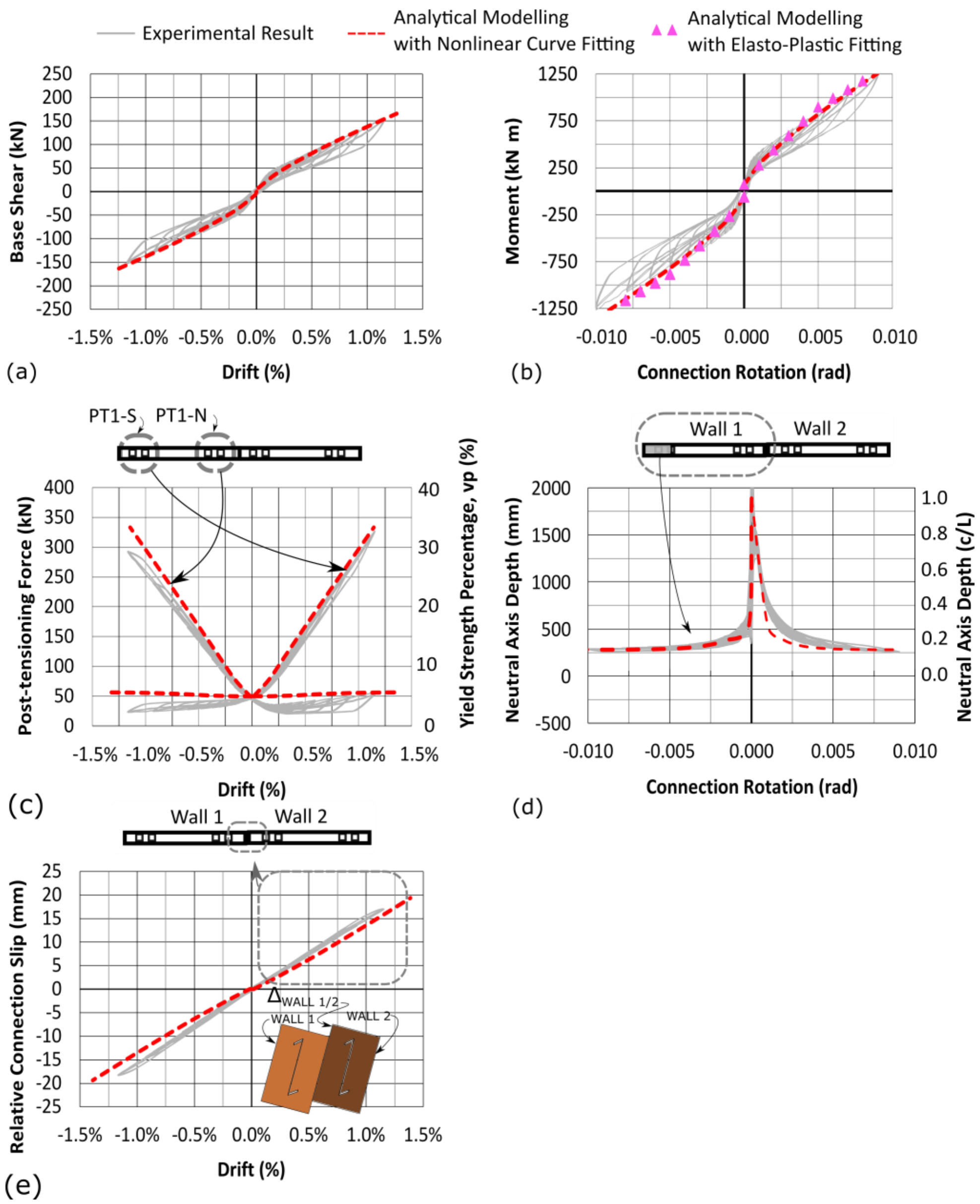


*Figure 21: Test DW-2 comparison to analytical model using both nonlinear and elasto-plastic curve fitting for STS in-plane joint*

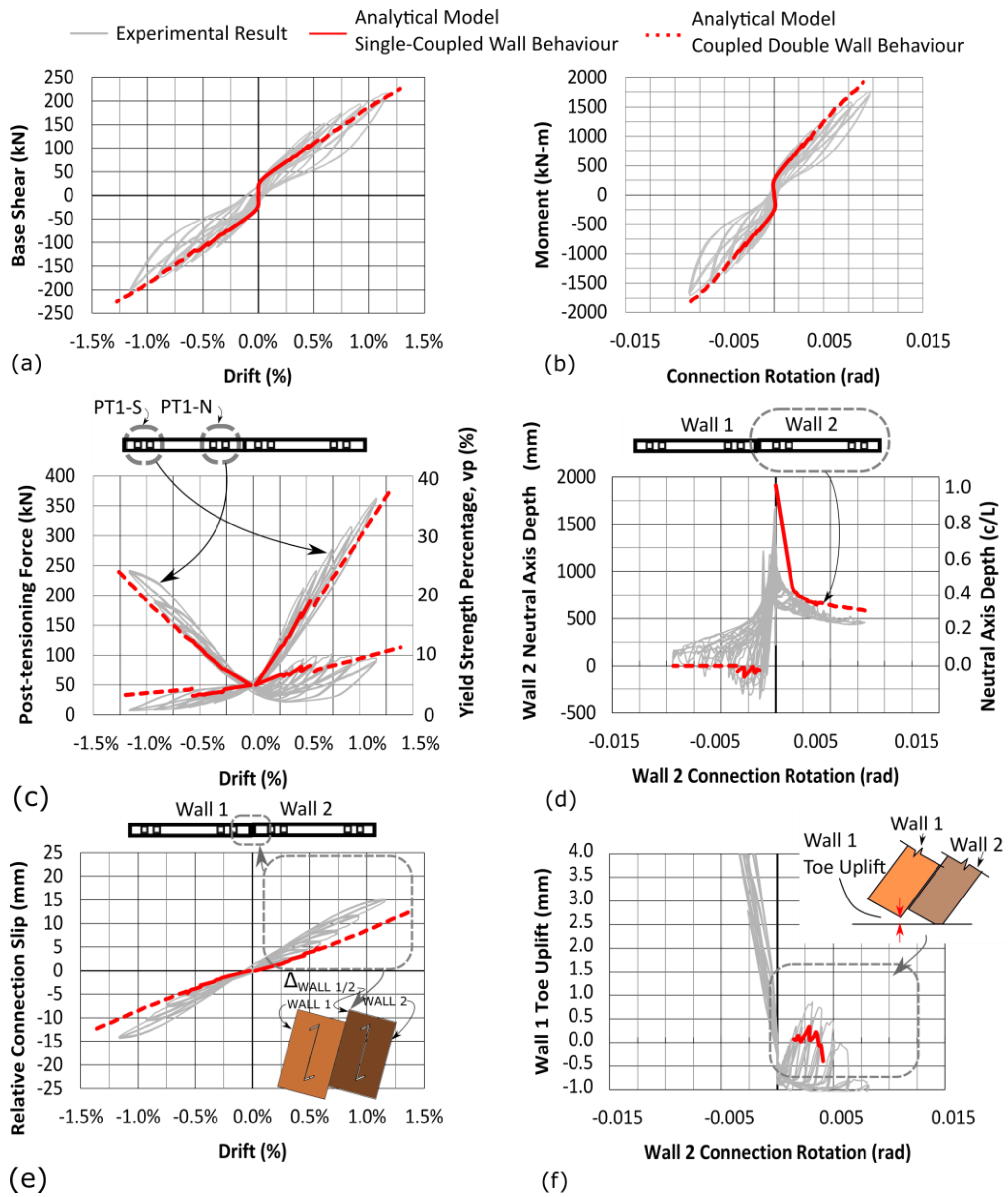


*Figure 22: Test DW-3 comparison to analytical model using nonlinear curve fitting for STS in-plane joint*

# 7 CONCLUSIONS AND RECOMMENDATIONS

This paper presented the experimental testing and the developed analytical models to assess the lateral cyclic behaviour of unbonded post-tensioned (PT) CLT Single Wall (SW) and Double Wall (DW) systems. The large-scale experimental test results showcased that PT CLT DW systems coupled with self-tapping screws (STS) could provide one effective solution to provide increased shear wall strength and stiffness while also providing stable performance and energy dissipation. Further, the proposed analytical prediction models were able to well predict the system level envelope curve responses of the CLT SW and DW systems with two different kinematic rocking modes. The key findings and recommendations are summarized as follows:

- With screwed connections, the PT double wall partial composite action of approximately 70% was achieved (Test DW-3) and the system stiffness was almost two times that of two PT single walls without partial composite action but equal wall length.
- The assumption of a triangular stress / strain distribution in the compressive toe at the wall base, which was originally validated with LVL, was experimentally verified as suitable by Particle Tracking Technology (PTT) when CLT is within the elastic range. Further work should investigate the strain behaviour beyond timber yielding with PTT to investigate if the triangular distribution is still valid.
- The Modified Monolithic Beam Analogy (MMBA) was verified for the post-tensioned (PT) CLT SW and DW systems. The test results showed the MMBA could under-predict the peak strain response in the compressive toe for the tested CLT walls due to the increased material variability and complexity when compared to LVL in past PT wall studies. A strain amplification factor ($\phi_t$) of 1.3 was determined for PT CLT wall systems. Future work is needed to investigate different wall configurations, drift demands, timber species and engineered timber products. The $\phi_t$ is thus preliminarily recommended for CLT that is non-edge glued and the lamella are visual stress graded.
- At the system level, the PT CLT SW moment-rotation behaviour was predicted with reasonable accuracy (within 15 % prediction error) when readily available material properties (i.e., from Building Codes, and supplier documentation) and the existing MMBA method were applied (without $\phi_t$). However, current analytical prediction methods for post-tensioned CLT walls may lead to an underestimation of the peak timber strain, thus leading to a slight overdesign of the reinforcement and reduction of the actual drift and strain level in the timber. Yet, should the target drift be reached at a higher intensity level, the predictive relationship between drift and local strain might lead to an underestimation of the local timber compression damage. The MMBA prediction error was reduced to 5 % when the component material properties and $\phi_t$ were applied.

- Extensions were made to the existing MMBA analytical model to well capture the envelope curve of PT Double Wall CLT systems coupled with Self-tapping Screws (STS) at the in-plane joint. The nonlinear curve fitting function proposed by Foschi [50] was employed to capture the entire load-displacement behaviour of the in-plane STS joint and unique wall uplift kinematic rocking mechanism (i.e., one wall base rocking interface). While the proposed method provided increased predictive accuracy than the elastoplastic curve fitting method by Iqbal et al. [24], future work should develop simplified methods for practitioners. The analytical model was limited to capturing the PT DW CLT system envelope curve and future work should implement hysteresis curve fitting models in order to model energy dissipation.
- It should be noted that a limited number of PT CLT shear wall experimental tests were performed with limited variation in some key design parameters such as initial PT force, STS in-plane joint details, and number of UFP elements. The tests were also performed on the same CLT wall specimens. Future work should also experimentally investigate PT CLT shear wall tests with different STS in-plane joint details such as half-lap joints with mixed angle STS combinations and then optimize the proposed PT CLT wall systems through a parametric/sensitivity analysis.

## 8 ACKNOWLEDGEMENTS

The authors would like to acknowledge the sponsorship of Speciality Wood Products Research Partnership, New Zealand Douglas-Fir Association, Australian Research Council Future Timber Hub, SPAX Pacific, BBR Contech, and the New Zealand Commonwealth Scholarship and Fellowship Plan. PTL Structural Consultants is acknowledged for the use of the Pres-Lam patent [87] in this research. The technical support from Peter Coursey, Russell McConchie, Alan Thirlwell, and Michael Weavers and technical comments from Dr. Daniel Moroder and Dr. Tobias Smith also are gratefully acknowledged.

## 9 LIST OF ABBREVIATIONS AND SYMBOLS

CDW Coupled double wall.

CLT Cross-Laminated Timber.

CLT5 Five-layer CLT.

DW Double wall.

ETA European technical approval.

LLRS Lateral load resisting system.

LVL Laminated veneer lumber.

LVDT Linear variable displacement transducer.

MMBA Modified monolithic beam analogy.

PT Post-tensioned.

PTH Partially threaded.

PTT Particle tracking technology.

RGB Red green blue.

SCW Single-coupled wall.

STS Self-tapping screw.

SLS Serviceability limit state.

SW Single wall.

UFP U-shaped flexural plate.

$\boldsymbol{a}$ Average width of the CLT lamella

$b_{eff}$ Sum of the longitudinal board thickness.

$A_{eff,wi}$ Effective cross-sectional area of the applicable CLT wall.

| | |
|---|---|
| $A_{PT,i}$ | Cross-section area of the i-th post-tensioning bar. |
| $b_u$ | UFP width. |
| $c_{i,j}$ | Wall 'i' neutral axis length for $\theta_j$ imposed base rotation angle. |
| $C_{T,i,j}$ | Timber compression force for the i-th Wall for $\theta_j$ imposed base rotation angle. |
| $d_{PT,i}$ | Edge distance of the i-th post-tensioning bar. |
| $d_{STS,fr,2}$ | Edge distance of the STS and friction force. |
| $d_{UFP,i}$ | Edge distance of the i-th UFP element. |
| $d_{2,f}$ | Final displacement of STS for Foschi model. |
| $d_{2,j}$ | Relative in-plane joint displacement for $\theta_j$ imposed base rotation angle. |
| $d_{2,u}$ | Displacement of STS at maximum force for the Foschi model.. |
| $D_u$ | Average radius of the UFP. |
| $E_{con}$ | Timber connection elastic modulus. |
| $E_D$ | Total energy dissipation. |
| $E_0$ | Modulus of elasticity parallel to the timber grain. |
| $E_{o-End}$ | Modulus of elasticity considering end effect of timber fibers. |
| $E_0 I_{eff,\gamma}$ | The effective flexural stiffness considering the 'gamma method'. |
| $E_{PT}$ | Post-tensioning bar modulus of elasticity. |
| $E_s$ | Mild steel modulus of elasticity. |
| $F_j$ | Force for $\theta_j$ imposed base rotation angle. |
| $f_c$ | Compression strength parallel to grain. |

| | |
|---|---|
| $F_{fr,2,j}$ | Friction force at the in-plane joint for $\theta_j$ imposed base rotation angle. |
| $F_{STS,2,j}$ | In-plane joint STS force for $\theta_j$ imposed base rotation angle. |
| $F_{STS,2,u}$ | Ultimate STS force parameter for the Foschi model. |
| $F_{UFP,i,j}$ | Yield force of UFP ‘i' for $\theta_j$ imposed base rotation angle. |
| $F_y$ | Yield strength. |
| $F_0$ | Foschi model parameter for force. |
| $G_0$ | Modulus of shear rigidity. |
| $G_{eff}$ | Effective shear modulus. |
| $H_{cant}$ | Wall height. |
| $I_{eff}$ | Second moment of inertia which considers $b_{eff}$. |
| k | Stiffness. |
| $k_{gap}$ | Factor which accounts for the ratio between $E_{o-End}$ and $E_0$. |
| $k_{PT,i,j}$ | Stiffness of the ‘i-th’ PT bar for $\theta_j$ imposed base rotation angle. |
| $k_{STS,2,j}$ | The stiffness of a single self-tapping screw fastener for a given displacement, $d_{2,j}$. |
| $K_{STS,2,j}$ | The total stiffness of the in-plane joint for a given displacement, $d_{2,j}$. |
| $k_{UFP,i,j}$ | Stiffness of the ‘i-th’ UFP element for $\theta_j$ imposed base rotation angle. |
| $K_0$ | Foschi model parameter for initial stiffness. |
| $L_i$ | Wall ‘i' length. |
| $l_{ub,i}$ | Unbonded length of the i-th post-tensioning bar. |
| $M_{conn,j}$ | Total base connection moment for $\theta_j$ imposed base rotation angle. |

| | |
|---|---|
| $M_{dec}$ | Decompression moment. |
| $M_{pt}$ | Base connection moment due to the post-tensioning bars. |
| $M_s$ | Base connection moment due to the dissipative elements. |
| $M_T$ | Total base connection moment. |
| $\mathrm{M}_{\mathrm{w,i,j}}$ | Base connection moment of the i-th wall for $\theta_j$ imposed base rotation angle. |
| $n_{STS,2}$ | The number of STS pairs along the in-plane joint. |
| $N$ | Axial force from gravity loading. |
| $r_1$ | Foschi model parameter for ascending branch |
| $r_2$ | Foschi model parameter for descending branch stiffness. |
| $\mathrm{t_b}$ | Average thickness of the CLT lamella. |
| $T_{PT,i,j}$ | Post-tensioning force in the i-th bar for $\theta_j$ imposed base rotation angle. |
| $T_{PT,0,i}$ | Initial post-tensioning force in the i-th bar. |
| $t_u$ | UFP thickness. |
| $Z$ | Elastic section modulus. |
| $\Delta_{PT,i,j}$ | Elongation of the i-th post-tensioning bar for $\theta_j$ imposed base rotation angle. |
| $\Delta_{UFP,i,j}$ | Elongation of the i-th UFP element for $\theta_j$ imposed base rotation angle. |
| $\delta$ | Wall drift. |
| $\delta_r$ | Rocking deformation component. |
| $\delta_b$ | Bending deformation component. |
| $\delta_s$ | Shear deformation component. |

| | |
|---|---|
| $\delta_T$ | Total deformation. |
| $\beta$ | Re-centring ratio. |
| $\varepsilon_t$ | Timber strain. |
| $\phi$ | Diameter. |
| $\phi_{dec}$ | Decompression curvature. |
| $\phi_t$ | Timber strain amplification factor. |
| $\psi$ | Friction co-efficient for wood-wood surfaces. |
| $\nu_{PT}$ | Yield percentage of the extreme PT bar. |
| $\nu_T$ | Yield strain percentage of the extreme timber fibre value. |
| $\omega_u$ | Displacement at maximum force as per Foschi model. |
| $\omega_f$ | Final displacement as per Foschi model. |
| $\theta_j$ | Wall base connection rotation. |
| $\sum T_{PT,wi,j}$ | Sum of post-tensioning bar force for the applicable wall, 'i', and wall base rotation 'j'. |
| $\sum T_{PT,o,wi,j}$ | Sum of the initial post-tensioning bar force for the applicable wall,i. |
| $F_{0\%,\delta}$ | The theoretical force for an uncoupled (non-composite) section. |
| $F_{100\%,\delta}$ | The theoretical force for a fully composite section. |
| $F_{Test,\delta}$ | The measured force. |
| $\%CA_\delta$ | The percentage composite action for a given drift level. |

723

## REFERENCES


[1] V. Kotradyova, E. Vavrinsky, B. Kalinakova, D. Petro, K. Jansakova, M. Boles, H. Svobodova, Wood and its impact on humans and environment quality in health care facilities, Int. J. Environ. Res. Public Health. 16 (2019). https://doi.org/10.3390/ijerph16183496.

[2] M. Green, The case for tall wood buildings: how mass timber offers a safe, economical, and environmentally friendly alternative for tall building structures, 2nd ed., MGA, British Columbia, 2017.

[3] S. Pei, J.W. Van De Lindt, M. Popovski, J.W. Berman, J.D. Dolan, J. Ricles, R. Sause, H. Blomgren, D.R. Rammer, Cross-Laminated Timber for Seismic Regions: Progress and Challenges for Research and Implementation, J. Struct. Eng. 142 (2016).

[4] J.W. van de Lindt, M.O. Amini, D. Rammer, P. Line, S. Pei, M. Popovski, Seismic Performance Factors for Cross-Laminated Timber Shear Wall Systems in the United States, J. Struct. Eng. 146 (2020) 1–16. https://doi.org/10.1061/(ASCE)ST.1943-541X.0002718.

[5] W. Dong, M. Li, L.M. Ottenhaus, H. Lim, Ductility and overstrength of nailed CLT hold-down connections, Eng. Struct. 215 (2020) 110667. https://doi.org/10.1016/j.engstruct.2020.110667.

[6] J.R. Brown, M. Li, F. Sarti, Structural performance of CLT shear connections with castellations and angle brackets, Eng. Struct. 240 (2021) 112346. https://doi.org/10.1016/j.engstruct.2021.112346.

[7] M. Li, R.O. Foschi, F. Lam, Modeling hysteretic behavior of wood shear walls with a protocol-independent nail connection algorithm, J. Struct. Eng. (United States). 138 (2012) 99–108. https://doi.org/10.1061/(ASCE)ST.1943-541X.0000438.

[8] M. Li, F. Lam, R.O. Foschi, S. Nakajima, T. Nakagawa, Seismic performance of post and beam timber buildings I: Model development and verification, J. Wood Sci. 58 (2012) 20–30. https://doi.org/10.1007/s10086-011-1219-5.

[9] M. Li, F. Lam, R.O. Foschi, S. Nakajima, T. Nakagawa, Seismic performance of post-and-beam timber buildings II: Reliability evaluations, J. Wood Sci. 58 (2012) 135–143. https://doi.org/10.1007/s10086-011-1232-8.

[10] M. Li, F. Lam, R.O. Foschi, Seismic reliability analysis of diagonal-braced and structural-panel-sheathed wood shear walls, J. Struct. Eng. 135 (2009) 587–596. https://doi.org/10.1061/(ASCE)ST.1943-541X.0000008.

[11] G. Flatscher, K. Bratulic, G. Schickhofer, Experimental tests on cross-laminated timber joints and walls, Proc. Inst. Civ. Eng. - Struct. Build. 168 (2015) 868–877. https://doi.org/10.1680/stbu.13.00085.

[12] L.-M. Ottenhaus, M. Li, T. Smith, Structural performance of large-scale dowelled CLT connections under monotonic and cyclic loading, Eng. Struct. 176 (2018) 41–48. https://doi.org/10.1016/j.engstruct.2018.09.002.

[13] J.R. Brown, M. Li, Structural performance of dowelled cross-laminated timber hold-down connections with increased row spacing and end distance, Constr. Build. Mater. 271 (2021) 121595. https://doi.org/10.1016/j.conbuildmat.2020.121595.

[14] A. Hashemi, P. Zarnani, P. Quenneville, Seismic assessment of rocking timber walls with energy dissipation devices, Eng. Struct. 221 (2020) 111053. https://doi.org/10.1016/j.engstruct.2020.111053.

[15] A. Buchanan, The challenges for designers of tall timber buildings, in: WCTE 2016 - World Conf. Timber Eng., Vienna, Austria, 2016.

[16] S. Pampanin, C. Christopoulos, M.J. Nigel Priestley, Performance-based seismic response of frame structures including residual deformations. Part II: Multi-degree of freedom systems, J. Earthq. Eng. 7 (2003) 119–147. https://doi.org/10.1080/13632460309350444.

[17] A. Palermo, S. Pampanin, A.H. Buchanan, M.P. Newcombe, Seismic design of multi-storey buildings using laminated veneer lumber (LVL), in: New Zeal. Soc. Earthq. Eng. Conf., 2005.

[18] A. Palermo, S. Pampanin, A.H. Buchanan, Experimental investigations on LVL seismic resistant wall and frame subassemblies, in: 1st Eur. Conf. Earthq. Eng. Seismol., Geneva, Switzerland, Sept 3-8, paper n.983, 2006.

[19] G. Granello, A. Palermo, S. Pampanin, S. Pei, J. Van De Lindt, Pres-Lam Buildings : State-of-the-Art, J. Struct. Eng. 146 (2020) 1–16. https://doi.org/10.1061/(ASCE)ST.1943-541X.0002603.

[20] L. Muszynski, Global CLT industry in 2020 : Growth beyond the Alpine Region, in: Proc. 63rd Int. Conv. Soc. Wood Sci. Technol., 2020 Pp. 1–8. Int. Conv. Soc. Wood Sci. Technol., 2020: pp. 1–8.

[21] F. Sarti, A. Palermo, S. Pampanin, Quasi-static cyclic testing of two-thirds scale unbonded post-tensioned rocking dissipative timber walls, J. Struct. Eng. 142 (2016) 1–14. https://doi.org/10.1061/(ASCE)ST.1943-541X.0001291.

[22] J.M. Kelly, R.I. Skinner, A.J. Heine, Mechanisms of energy absorption in special devices for use in earthquake resistant structures, Bull. New Zeal. Soc. Earthq. Eng. 5 (1972) 63–73.

[23] A. Iqbal, S. Pampanin, A. Palermo, A.H. Buchanan, Performance and design of LVL walls coupled with UFP dissipaters, J. Earthq. Eng. 19 (2015) 383–409. https://doi.org/10.1080/13632469.2014.987406.

[24] A. Iqbal, T. Smith, S. Pampanin, M. Fragiacomo, A. Palermo, A.H. Buchanan, Experimental performance and structural analysis of plywood-coupled LVL walls, J. Struct. Eng. 142 (2015).

[25] A. Dunbar, D. Moroder, S. Pampanin, A. Buchanan, Timber core-walls for lateral load resistance of multi-storey timber buildings, in: World Conf. Timber Eng., 2014.

[26] R. Ganey, J. Berman, T. Akbas, S. Loftus, J. Daniel Dolan, R. Sause, J. Ricles, S. Pei, J.V.D. Lindt, H.E. Blomgren, Experimental investigation of self-centering Cross-Laminated Timber walls, J. Struct. Eng. 143 (2017).

[27] D. Moroder, T. Smith, A. Dunbar, S. Pampanin, A. Buchanan, Seismic testing of post-tensioned Pres-Lam core walls using cross laminated timber, Eng. Struct. 167 (2018) 639–654. https://doi.org/10.1016/j.engstruct.2018.02.075.

[28] T. Smith, F.C. Ponzo, A. Di Cesare, S. Pampanin, D. Carradine, A.H. Buchanan, D. Nigro, Post-tensioned glulam beam-column joints with advanced damping systems: Testing and numerical analysis, J. Earthq. Eng. 18 (2014) 147–167. https://doi.org/10.1080/13632469.2013.835291.

[29] A. Di Cesare, F.C. Ponzo, D. Nigro, S. Pampanin, T. Smith, Shaking table testing of post-tensioned timber frame building with passive energy dissipation systems, Bull. Earthq. Eng. 15 (2017) 4475–

4498. https://doi.org/10.1007/s10518-017-0115-9.

[30] T. Nagashima, K. Tachibana, M. Yano, Y. Ohashi, Design Method for Post-Tensioned timber Shear wall - triangular embedment and behaviour in elastic range, AIJ. 85 (2020) 539–549. https://doi.org/10.1017/CBO9781107415324.004.

[31] S. Bianchi, J. Ciurlanti, A.C. Costa, S. Pampanin, D. Perrone, P.X. Candeias, Shake-table tests of innovative drift sensitive nonstructural elements in a low-damage structural system, Earthq. Eng. Struct. Dyn. (2021) 1–23. https://doi.org/https://doi.org/10.1002/eqe.3452.

[32] M.J. Mancini, S. Pampanin, Numerical and Experimental Investigation on Low Damage Steel-Timber Post-Tensioned Beam-Column Connection, in: 16th Eur. Conf. Earthq. Eng., 2018: pp. 1–12.

[33] S. Pei, J.W. van de Lindt, J. Ricles, R. Sause, J. Berman, K. Ryan, J.D. Dolan, A. Buchanan, T. Robinson, E. McDonnell, Development and Full-Scale Validation of Resilience-Based Seismic Design of Tall Wood Buildings: The NHERI Tallwood Project, in: Proc. New Zeal. Soc. Earthq. Eng. Annu. Conf. April 27-29, Wellington, New Zealand, 2017, 2017.

[34] S. Pei, J.W. Van De Lindt, A.R. Barbosa, J.W. Berman, E. McDonnell, J. Daniel Dolan, H.E. Blomgren, R.B. Zimmerman, D. Huang, S. Wichman, Experimental seismic response of a resilient 2-story mass-timber building with post-tensioned rocking walls, J. Struct. Eng. 145 (2019) 1–15.

[35] Z. Chen, M. Popovski, A. Iqbal, Structural Performance of Post-Tensioned CLT Shear Walls with Energy Dissipators, J. Struct. Eng. 146 (2020). https://doi.org/10.1061/(asce)st.1943-541x.0002569.

[36] X. Sun, M. He, Z. Li, Experimental and Analytical Lateral Performance of Posttensioned CLT Shear Walls and Conventional CLT Shear Walls, J. Struct. Eng. (United States). 146 (2020) 1–15. https://doi.org/10.1061/(ASCE)ST.1943-541X.0002638.

[37] P. Dietsch, R. Brandner, Self-tapping screws and threaded rods as reinforcement for structural timber elements-A state-of-the-art report, Constr. Build. Mater. 97 (2015) 78–89. https://doi.org/10.1016/j.conbuildmat.2015.04.028.

[38] C. Loss, A. Hossain, T. Tannert, Simple cross-laminated timber shear connections with spatially

arranged screws, Eng. Struct. 173 (2018) 340–356. https://doi.org/10.1016/j.engstruct.2018.07.004.

[39] A. Hossain, M. Popovski, T. Tannert, Cross-laminated timber connections assembled with a combination of screws in withdrawal and screws in shear, Eng. Struct. 168 (2018) 1–11. https://doi.org/10.1016/j.engstruct.2018.04.052.

[40] J.R. Brown, M. Li, T. Tannert, D. Moroder, Experimental study on orthogonal joints in cross-laminated timber with self-tapping screws installed with mixed angles, Eng. Struct. 228 (2021) 111560. https://doi.org/10.1016/j.engstruct.2020.111560.

[41] K. Sullivan, T.H. Miller, R. Gupta, Behavior of cross-laminated timber diaphragm connections with self-tapping screws, Eng. Struct. 168 (2018) 505–524.

[42] S. Pampanin, M.J. Nigel Priestley, S. Sritharan, Analytical modelling of the seismic behaviour of precast concrete frames designed with ductile connections, J. Earthq. Eng. 5 (2001) 329–367. https://doi.org/10.1080/13632460109350397.

[43] A. Palermo, Use of controlled rocking in the seismic design of bridges, Technical University of Milan, 2004.

[44] M.P. Newcombe, S. Pampanin, A. Buchanan, A. Palermo, Section analysis and cyclic behavior of post-tensioned jointed ductile connections for multi-story timber buildings, J. Earthq. Eng. 12 (2008) 83–110. https://doi.org/10.1080/13632460801925632.

[45] M.P. Newcombe, Seismic design of multistorey post-tensioned timber buildings, University of Pavia, Pavia, Italy, 2008.

[46] T. Smith, F. Ludwig, S. Pampanin, M. Fragiacomo, A. Buchanan, B. Deam, A. Palermo, Seismic response of hybrid-LVL coupled walls under quasi-static and pseudo-dynamic testing, in: 2007 New Zeal. Soc. Earthq. Eng. Conf. Palmerst. North, New Zeal., 2007.

[47] R. Nokes, Streams 3.02: System Theory and Design, 2019.

[48] T. Akbas, R. Sause, J.M. Ricles, R. Ganey, J. Berman, S. Loftus, J.D. Dolan, S.L. Pei, J.W. van de Lindt, H.E. Blomgren, Analytical and Experimental Lateral-Load Response of Self-Centering

Posttensioned CLT Walls, J. Struct. Eng. 143 (2017). https://doi.org/10.1061/(asce)st.1943-541x.0001733.

[49] I. Gavric, M. Fragiacomo, A. Ceccotti, Cyclic behavior of CLT wall systems: experimental tests and analytical prediction models, J. Struct. Eng. 141 (2015) 4015034. https://doi.org/doi:10.1061/(ASCE)ST.1943-541X.0001246.

[50] R.O. Foschi, Analysis of wood diaphragms and trusses, Part 1: Diaphragms, Can. J. Civ. Eng. 4 (1977) 345–362.

[51] B. Folz, A. Filiatrault, Cyclic analysis of wood shear walls, J. Struct. Eng. 127 (2001) 433–441.

[52] J.R. Brown, M. Li, A. Palermo, S. Pampanin, F. Sarti, Experimental Testing of a Low-Damage post-tensioned C-Shaped CLT Core-Wall, J. Struct. Eng. 147 (2021) 1–16. https://doi.org/10.1061/(ASCE)ST.1943-541X.0002926.

[53] J.R. Brown, Seismic Performance of CLT Core-Wall Systems and Connections, University of Canterbury, 2021. https://doi.org/http://dx.doi.org/10.26021/11438.

[54] Standards New Zealand, NZS 3603: Timber structures standard, Standards New Zealand, Private Bag 2439, Wellington, New Zealand, 1993.

[55] CEN, Eurocode 5: Design of timber structures-Part 1-1: General-Common rules and rules for buildings, EN1995-1-12004-11 + AC2006-06 + A12008-06 + A22014-05 Eurocode 5. (2014).

[56] ETA-12/0114, SPAX self-tapping screws- screws for use in timber constructions, ETA-Danmark A/S, 2017.

[57] ETA-07/0046, ETA-07/0046: Macalloy 1030 post tensioning system, European Technical Approval, Charlottenlund, Denmark, 2018.

[58] A. Baird, T. Smith, A. Palermo, S. Pampanin, Experimental and numerical Study of U-shape Flexural Plate ( UFP ) dissipators, NZSEE Conf. (2014) 1–9.

[59] ETA-11/0030, Rotho Blass Self-tapping screws and threaded rods, ETA-Danmark A/S, 2019.

[60] Standards New Zealand, NZS 3404: Steel Structures Standard, Standards New Zealand, Private Bag 2439, Wellington, New Zealand, 1992.

[61] ConcreteNZ, Lucas House, Nelson, (2015). http://www.concretesociety.org.nz/index.php/concrete-awards/awards-2015/26-awards-2015/223-lucas-house-other-entrants (accessed August 10, 2021).

[62] Australian / New Zealand Standard, AS/NZS 3679: Steel reinforcing materials, In: Standards Australia, GPO Box 476, Sydney, NSW and Standards New Zealand, Private Bag 2439, Wellington, New Zealand, 2016.

[63] A. Palermo, F. Sarti, A. Baird, D. Bonardi, D. Dekker, S. Chung, From theory to practice: Design, analysis and construction of dissipative timber rocking post-tensioning wall system for Carterton Events Centre, New Zealand, Proc. 15th World Conf. Earthq. Eng. Lisbon, Port. (2012) 24–28.

[64] ACI Innovation Task Group 5, Acceptance criteria for special unbonded post-tensioned precast structural walls based on validation testing and commentary : an ACI standard, (2008).

[65] L.-M. Ottenhaus, M. Li, R. Nokes, P. Cammock, B. McInnes, Use of particle tracking velocimetry in timber material and connection testing, Eur. J. Wood Wood Prod. 77 (2019) 195–209. https://doi.org/10.1007/s00107-018-1376-y.

[66] J. Brown, M. Li, R. Nokes, A. Palermo, S. Pampanin, F. Sarti, Investigating the compressive toe of pos-tensioned CLT core-walls use Particle Tracking Technology, in: 17th World Conf. Earthq. Eng. 17WCEE, Sendai, Japan, 2020.

[67] Australian / New Zealand Standard, AS/NZS 1170.0 Structural Design Actions Part 0: General Principles, In: Standards Australia, GPO Box 476, Sydney, NSW and Standards New Zealand, Private Bag 2439, Wellington, New Zealand, 2002.

[68] J. Brown, M. Li, A. Palermo, S. Pampanin, F. Sarti, Bi-Directional Seismic Testing of Post-Tensioned Rocking CLT Walls and Core-Walls, in: WCTE 2021, Santiago, Chile, 2021.

[69] J. Pault, R. Gutkowski, Tests and analysis of composite action in glulam bridges', Structural Research report No. 17A, Ft. Collins, CO., 1977.

[70] S. Pampanin, A. Palermo, A. Buchanan, Post-Tensioned Timber Buildings - Design Guide Australia and New Zealand, Structural Timber Innovation Company, Christchurch, 2013.

[71] A. Iqbal, M. Fragiacomo, S. Pampanin, A. Buchanan, Seismic resilience of plywood-coupled LVL wall panels, Eng. Struct. 167 (2018) 750–759. https://doi.org/10.1016/j.engstruct.2017.09.053.

[72] A. Hossain, Experimental investigations of shear connection with STS for CLT panels, University of British Columbia, 2019. https://doi.org/.1037//0033-2909.I26.1.78.

[73] R.I. Skinner, J.M. Kelly, A.J. Heine, Hysteretic dampers for earthquake-resistant structures, Earthq. Eng. Struct. Dyn. 3 (1974) 287–296. https://doi.org/10.1002/eqe.4290030307.

[74] W. Ramberg, W.R. Osgood, Description of stress-strain curves by three parameters, Washington, D.C., 1943.

[75] R.O. Foschi, Load-slip characteristics of nails, Wood Sci. 7 (1974) 69–74.

[76] T. Holden, C. Devereux, S. Haydon, A. Buchanan, S. Pampanin, NMIT Arts and Media Building—Innovative structural design of a three storey post-tensioned timber building, Case Stud. Struct. Eng. 6 (2016) 76–83. https://doi.org/10.1016/j.csse.2016.06.003.

[77] M. Shahnewaz, M. Popovski, T. Tannert, Deflection of cross-laminated timber shear walls for platform-type construction, Eng. Struct. 221 (2020) 111091. https://doi.org/10.1016/j.engstruct.2020.111091.

[78] M. Izzi, D. Casagrande, S. Bezzi, D. Pasca, M. Follesa, R. Tomasi, Seismic behaviour of Cross-Laminated Timber structures: A state-of-the-art review, Eng. Struct. 170 (2018) 42–52. https://doi.org/10.1016/j.engstruct.2018.05.060.

[79] FPInnovations, CLT Handbook, FPInnovations, Pointe-Claire, QC, 2019.

[80] I. Lukacs, A. Björnfot, R. Tomasi, Strength and stiffness of cross-laminated timber (CLT) shear walls: State-of-the-art of analytical approaches, Eng. Struct. 178 (2019) 136–147. https://doi.org/10.1016/j.engstruct.2018.05.126.

[81] G. Schickhofer, T. Bogensperger, T. Moosbrugger, M. Augustin, H.J. Blaß, E. H, et al., BSPhandbuch, Holz- Massivbauweise in Brettsperrholz, Technische Universitat Graz, Karlsruher Institut fur

Technologie, 2010.

[82] CEN, EN 408:2010+A1:2012, European Committee for Standardization (CEN), Brussels, Belgium, 2012.

[83] Australian / New Zealand Standard, AS/NZS 4671: Steel reinforcing materials, In: Standards Australia, GPO Box 476, Sydney, NSW and Standards New Zealand, Private Bag 2439, Wellington, New Zealand, 2001.

[84] EN ISO 6892-1, Metallic materials — Tensile testing Part 1 : Method of test at room temperature, European Committee for Standardization, Brussels, Belgium, 2016.

[85] M.A. Kovacs, Design of controlled rocking heavy timber walls for low-to-moderate seismic Hazard Regions, Master Thesis - McMaster University, 2016.

[86] P. Deng, S. Pei, J.W. van de Lindt, M. Omar Amini, H. Liu, Lateral behavior of panelized CLT walls: A pushover analysis based on minimal resistance assumption, Eng. Struct. 191 (2019) 469–478. https://doi.org/10.1016/j.engstruct.2019.04.080.

[87] A. Buchanan, S. Pampanin, A. Palermo, An engineering wood construction system for high performance structures using pre-stressed tendons and replaceable energy dissipaters- New Zealand Patent No. 549029 Australia Patent No. 2007282232, 549029, 2006.